



An Asymmetric Eclipse Seen toward the Pre-main-sequence Binary System V928 Tau

Dirk M. van Dam¹, Matthew A. Kenworthy¹, Trevor J. David^{2,3}, Eric E. Mamajek^{3,4}, Lynne A. Hillenbrand⁵, Ann Marie Cody⁶, Andrew W. Howard⁵, Howard Isaacson^{7,8}, David R. Ciardi⁹, Luisa M. Rebull¹⁰, John R. Stauffer¹¹, Rahul Patel¹², Andrew Collier Cameron + WASP Collaborators¹³, Joseph E. Rodriguez¹⁴, Grzegorz Pojmański¹⁵, Erica J. Gonzales^{16,23}, Joshua E. Schlieder¹⁷, Franz-Josef Hamsch^{18,19}, Sjoerd Dufoer¹⁹, Tonny Vanmunster^{18,20,21}, Franky Dubois^{18,19,22}, Siegfried Vanaverbeke^{18,19,22}, Ludwig Logie²², and Steve Rau²²

¹ Leiden Observatory, Leiden University, P.O. Box 9513, 2300 RA Leiden, The Netherlands; dmvandam@strw.leidenuniv.nl

² Center for Computational Astrophysics, Flatiron Institute, New York, NY 10010, USA

³ Jet Propulsion Laboratory, California Institute of Technology, 4800 Oak Grove Drive, Pasadena, CA 91109, USA

⁴ Department of Physics & Astronomy, University of Rochester, Rochester, NY 14627, USA

⁵ Department of Astronomy, California Institute of Technology, Pasadena, CA 91125, USA

⁶ Bay Area Environmental Research Institute, 625 2nd Street, Ste. 209, Petaluma, CA 94952, USA

⁷ 501 Campbell Hall, University of California at Berkeley, Berkeley, CA 94720, USA

⁸ Centre for Astrophysics, University of Southern Queensland, Toowoomba, QLD, Australia

⁹ California Institute of Technology/IPAC-NASA Exoplanet Science Institute, Pasadena, CA 91125, USA

¹⁰ Infrared Science Archive (IRSA), IPAC, 1200 E. California Boulevard, California Institute of Technology, Pasadena, CA 91125, USA

¹¹ Spitzer Science Center (SSC), IPAC, 1200 E. California Boulevard, California Institute of Technology, Pasadena, CA 91125, USA

¹² Infrared Processing and Analysis Center, California Institute of Technology, Pasadena, CA 91125, USA

¹³ Centre for Exoplanet Science, SUPA, School of Physics and Astronomy, University of St Andrews, St Andrews KY16 9SS, UK

¹⁴ Center for Astrophysics | Harvard & Smithsonian, 60 Garden Street, Cambridge, MA 02138, USA

¹⁵ Astronomical Observatory, University of Warsaw, Al. Ujazdowskie 4, 00-478 Warszawa, Poland

¹⁶ Department of Astronomy & Astrophysics, University of California, Santa Cruz, CA 95064, USA

¹⁷ NASA Goddard Space Flight Center, 8800 Greenbelt Road, Greenbelt, MD 20771, USA

¹⁸ American Association of Variable Star Observers (AAVSO), 49 Bay State Road, Cambridge, MA 02138, USA

¹⁹ Vereniging Voor Sterrenkunde (VVS), Oostmeers 122 C, B-8000 Brugge, Belgium

²⁰ CBA Belgium Observatory, Walhostraat 1A, B-3401 Landen, Belgium

²¹ CBA Extremadura Observatory, E-06340 Fregenal de la Sierra, Badajoz, Spain

²² Astrolab IRIS, Verbrandemolenstraat, Ypres, Belgium

Received 2020 July 18; revised 2020 October 14; accepted 2020 October 17; published 2020 November 26

Abstract

K2 observations of the weak-lined T Tauri binary V928 Tau A and B show the detection of a single, asymmetric eclipse, which may be due to a previously unknown substellar companion eclipsing one component of the binary with an orbital period >66 days. Over an interval of about 9 hr, one component of the binary dims by around 60%, returning to its normal brightness about 5 hr later. From modeling of the eclipse shape, we find evidence that the eclipsing companion may be surrounded by a disk or a vast ring system. The modeled disk has a radius of $0.9923 \pm 0.0005 R_*$, with an inclination of $56^\circ.78 \pm 0^\circ.03$, a tilt of $41^\circ.22 \pm 0^\circ.05$, an impact parameter of $-0.2506 \pm 0.0002 R_*$, and an opacity of 1.00. The occulting disk must also move at a transverse velocity of $6.637 \pm 0.002 R_* \text{ day}^{-1}$, which, depending on whether it orbits V928 Tau A or B, corresponds to approximately 73.53 or 69.26 km s^{-1} . A search in ground-based archival data reveals additional dimming events, some of which suggest periodicity, but no unambiguous period associated with the eclipse observed by K2. We present a new epoch of astrometry that is used to further refine the orbit of the binary, presenting a new lower bound of 67 yr, and constraints on the possible orbital periods of the eclipsing companion. The binary is also separated by $18''$ (~ 2250 au) from the lower-mass CFHT-BD-Tau 7, which is likely associated with V928 Tau A and B. We also present new high-dispersion optical spectroscopy that we use to characterize the unresolved stellar binary.

Unified Astronomy Thesaurus concepts: Planetary rings (1254); Pre-main sequence stars (1290); Astrometric binary stars (79); Eclipses (442); Substellar companion stars (1648)

1. Introduction

With the advent of high-precision photometric telescopes from the ground and space, astronomers have been able to continuously observe a large number of stars that exhibit intriguing behavior in their apparent brightness. This can come from intrinsic stellar variability, i.e., high-amplitude optical variability of young stars (Joy 1945), rotational starspot modulation (Rodono et al. 1986; Olah et al. 1997), asteroseismology (Handler 2013), or from interactions with objects or dust orbiting the star. “Dipper” stars are a class of stars where occultations due to dust in the inner boundaries of circumstellar disks produce transits with depths of

up to 50% (Alencar et al. 2010; Cody et al. 2014; Cody & Hillenbrand 2018). Ansdell et al. (2019a) found that in some cases, this requires misalignment of the inner protoplanetary disk compared to the circumstellar disk, and Ansdell et al. (2019b) found that shallower dips could be caused by exocomets. A particular system of interest, due to its evolved age, is RZ Psc, studied by Kennedy et al. (2017), which is a Sun-like star exhibiting transits of dust clumps, that could originate from an asteroid belt analog of the solar system. Other intriguing transits include disintegrating planets, which have regular periods but varying transit depths due to the loss of planetary material (Rappaport 2012; van Lieshout & Rappaport 2018; Ridden-Harper et al. 2018).

²³ National Science Foundation Graduate Research Fellow.

An additional source of deep asymmetric eclipses, which we will explore further in this study, is the transit of tilted and inclined circum“planetary” disks, which, due to projection effects, create elliptical occulters. These systems are interesting as they reveal the formation mechanism of planets, particularly if we observe young systems. Circumstellar disks are a fundamental feature of stellar formation, and the planets that form in these disks are influenced by the structure and composition of the protoplanetary disk, the interaction with the young host star, and the different formation mechanisms of planets (see reviews by Armitage 2011; Kley & Nelson 2012). Direct imaging allows astronomers to study the general size, shape, and composition of these circum“planetary” disks, but the transit method allows the spatial structure to be probed indirectly with a resolution significantly higher than through direct imaging. Besides providing insight into planet formation, these systems also reveal the mechanisms of ring and moon formation (Teachey et al. 2018). Other systems that have been explored include EPIC 204376071 (Rappaport et al. 2019), 1SWASP J140745.93–394542.6J1407 (J1407, Kenworthy & Mamajek 2015), and PDS 110 (Osborn et al. 2017, 2019).

The Kepler space telescope (Borucki et al. 2010) was designed to determine the frequency of Earth-sized planets in and near the habitable zone of Sun-like stars, η_{Earth} , which as a consequence produced a large number of high-precision light curves. After the failure of the second of its four reaction wheels, the mission was reconfigured to the extended K2 mission (Howell et al. 2014), which observed fields along the ecliptic. K2 has found several of these deep asymmetric eclipses, which have been compiled into a comprehensive list by LaCourse & Jacobs (2018). Here we present K2 observations of the pre-main-sequence binary star V928 Tau which shows a deep and asymmetric eclipse, potentially due to a previously unknown companion orbiting one component of the binary. The nature of the source of extinction is unknown, but consistent with a small dust disk.

In Section 2, we present and determine the properties of V928 Tau. Section 3 describes all the observations of the system from photometry, spectroscopy, astrometry, to high-resolution imaging. Section 4 describes all the analysis performed on the K2 light curve. This includes the modeling of the stellar variation and the eclipse, and a periodicity search. We summarize and discuss our findings in Section 6. The preliminary results for this system were presented in van Dam et al. (2019).

2. Stellar Characterization

2.1. Literature

The current state of published knowledge about V928 Tau is summarized in Table 1 and in succeeding subsections.

Membership Provenance: V928 Tau is a proposed member of the Taurus-Auriga star-forming complex ($d \sim 145$ pc, $\tau \sim 0\text{--}5$ Myr). The star’s membership was first proposed by Jones & Herbig (1979) on the basis of proper motions, and it was given the designation JH 91. Other aliases include L1529-23, EPIC 247795097, and HBC 398.

Environment: V928 Tau is located in the TMC 2 region of the dark cloud complex B18 (Kutner’s cloud, Leinert et al. 1993) and belongs to the Tau IV subgroup (Gomez et al. 1993; Luhman et al. 2009). The star is separated by $18''$ from another Tau-Aur member, CFHT-BD-Tau 7 (2MASS J04321786+2422149, EPIC

Table 1
Parameters of V928 Tau

Parameter	Value (primary, secondary)	References
<i>Kinematics and position</i>		
R.A., J2000 (hh mm ss)	04 32 18.88	Gaia DR2
Decl., J2000 (dd mm ss)	+24 22 26.71	Gaia DR2
μ_{α} (mas yr ⁻¹)	18.6 ± 5.1	Zacharias et al. (2015)
μ_{δ} (mas yr ⁻¹)	-21.2 ± 5.1	Zacharias et al. (2015)
v_R (km s ⁻¹)	15.38 ± 0.16	Nguyen et al. (2012)
ϖ (mas)	8.0534 ± 0.1915	Gaia DR2—CFHT-BD-Tau 7
Distance (pc)	124 ± 3	Gaia DR2—CFHT-BD-Tau 7
<i>Photometry</i>		
u (mag)	18.000 ± 0.012	SDSS DR12
g (mag)	15.367 ± 0.004	SDSS DR12
r (mag)	14.772 ± 0.011	SDSS DR12
i (mag)	15.841 ± 0.014	SDSS DR12
z (mag)	12.619 ± 0.011	SDSS DR12
G (mag)	12.8122 ± 0.0018	Gaia DR2
G_{BP} (mag)	14.3086 ± 0.0078	Gaia DR2
G_{RP} (mag)	11.6026 ± 0.0045	Gaia DR2
J (mag)	9.538 ± 0.020	2MASS
H (mag)	8.432 ± 0.021	2MASS
K_s (mag)	8.106 ± 0.021	2MASS
$W1$ (mag)	7.906 ± 0.023	WISE—All-Sky
$W2$ (mag)	7.804 ± 0.019	WISE—All-Sky
$W3$ (mag)	7.717 ± 0.022	WISE—All-Sky
$W4$ (mag)	7.705 ± 0.294	WISE—All-Sky
<i>Deblended Photometry</i>		
J (mag)	$10.23 \pm 0.03,$ 10.35 ± 0.03	this work
K_s (mag)	$8.82 \pm 0.02,$ 8.89 ± 0.02	this work
<i>Dereddened Photometry</i>		
J_0 (mag)	$9.77 \pm 0.05,$ 9.90 ± 0.05	this work
$K_{s,0}$ (mag)	$8.64 \pm 0.03,$ 8.67 ± 0.03	this work
<i>Physical properties</i>		
Spectral type	$M0.8 \pm 0.5$	Hecceg & Hillenbrand (2014)
A_V (mag)	1.95 ± 0.2	Hecceg & Hillenbrand (2014)
$E(B - V)$ (mag)	0.63 ± 0.07	this work
T_{spec} (K)	$3660 \pm 70,$ 3660 ± 70	this work
T_{phot} (K)	$3610 \pm 110,$ 3640 ± 110	this work
$\log(L_*/L_{\odot})$ (dex)	$-0.518 \pm 0.031,$ -0.570 ± 0.032	this work
R_* (R_{\odot})	$1.376 \pm 0.059,$ 1.296 ± 0.056	this work
M_* (M_{\odot})	$0.70 \pm 0.07,$ 0.70 ± 0.07	this work—DMM
	$0.45 \pm 0.05,$ 0.46 ± 0.05	this work—DSM
τ_* (Myr)	$5.8 \pm 1.5, 6.9 \pm 1.8$ $2.5 \pm 0.6, 3.0 \pm 0.7$	this work—DMM this work—DSM
$v \sin i_*$ (km s ⁻¹)	29 ± 3 33.1 ± 1.2 34.2 ± 0.4 31.6 ± 0.7 18.8 ± 3.3	this work—2017 spectrum this work—2018 spectrum Kounkel et al. (2019) Nguyen et al. (2012)
	24.9	Hartmann & Stauffer (1989)
EW(H α) (Å)	-0.95	Hartmann et al. (1986) this work

Table 1
(Continued)

Parameter	Value (primary, secondary)	References
EW(H β) (Å)	−0.89	this work
EW(Ca II H) (Å)	−8.9	this work
EW(Ca II K) (Å)	−13.4	this work
EW(Li I 6707.8) (mÅ)	658	this work
	639	Martin et al. (1994)
$P_{\text{rot},1}$ (d) ^a	2.25	this work
$P_{\text{rot},2}$ (d)	2.48	this work

References. 2MASS = Skrutskie et al. (2006); Gaia DR2 = Gaia Collaboration et al. (2018); SDSS DR12 = Alam et al. (2015); WISE—All-Sky = Wright et al. (2010). DMM = Dartmouth Magnetic Models (Feiden 2016), DSM = Dartmouth Standard Models (Dotter et al. 2008).

^a $P_{\text{rot},1}$ could correspond to either V928 Tau A or B, meaning $P_{\text{rot},2}$ corresponds to the remaining star.

247794636), which resides in the same K2 postage stamp. Statistical analysis of the spatial distribution of Taurus members suggests that stars this close ($18''18 \simeq 2250$ au at a distance of 124 pc) are almost certainly physical multiples (Gomez et al. 1993; Joncour et al. 2017, 2018). Astrometric information on the environment of V928 Tau is summarized in Table 2.

Binarity: V928 Tau was first discovered to be a binary through lunar occultation observations at $2.2 \mu\text{m}$ and followed up with speckle imaging, which revealed the two stars to be closely separated on the sky ($\rho \approx 0''.2$) and nearly equal in brightness at the K band (Leinert et al. 1993). Schaefer et al. (2014) analyzed the astrometric motion of the binary V928 Tau based on newly acquired Keck NIRC2 data and previously published measurements from the literature (Ghez et al. 1993, 1995; Leinert et al. 1993; Simon et al. 1996; White & Ghez 2001; Kraus & Hillenbrand 2012). From the compilation of measurements, those authors found that the projected motion of the binary could not be distinguished from linear motion. However, assuming the pair is bound, those authors found that an orbital period greater than 58 yr was required to fit the data. Kraus & Hillenbrand (2012) characterized the binary further, deriving a mass ratio of $q = 0.97$, individual masses of $M_1 = 0.60 M_\odot$ and $M_2 = 0.58 M_\odot$, and projected separation of 32 au. The likely association with CFHT-BD-Tau 7 at $\simeq 2250$ au has been proposed in Guieu et al. (2006) and explored further in Kraus & Hillenbrand (2009). The multiplicity is explored further in Joncour et al. (2018), where V928 Tau and CFHT-BD-Tau 7 are in NEST 9.

Circumstellar Disk: The star is a weak-lined T Tauri with modest H α emission ($\text{EW}(\text{H}\alpha) = -1.2$ to -2.4 Å Cohen & Kuhl 1979; Feigelson & Kriss 1983; Kenyon et al. 1998; Dent et al. 2013; this work) and a class III spectral energy distribution ($L_{\text{FIR}}/L_{\text{bol}} < 0.04$; Kenyon et al. 1998). The state of a putative disk has been studied numerous times over the years, beginning with Strom et al. (1989). Recently, Dent et al. (2013) estimated an upper limit to the mass of dust within the system of $< 4 \times 10^{-6} M_\odot$.

Spectral Type: An initial spectral classification of M0.5 was determined for this star by Cohen & Kuhl (1979), and Feigelson & Kriss (1983) quoted K7/M0e. From a flux-calibrated, low-resolution optical spectrum of V928 Tau, Herczeg & Hillenbrand (2014) determined a more precise combination of spectral type (M0.8), V -band extinction (1.95 mag), and veiling at 7510 \AA

(0.00). Those authors also used the Tognelli et al. (2011) evolutionary models to determine the stellar mass ($0.5 M_\odot$) and age (1.6 Myr), under the assumption of a single star. Tottle & Mohanty (2015) fit model atmospheres to the spectral energy distribution of V928 Tau, finding $T_{\text{eff}} = 3525$ K, $A_J = 0.94$ mag, and $\log L/L_\odot = 1.04$. Kounkel et al. (2019) determined from an analysis of H -band spectra a somewhat warmer temperature of $T_{\text{eff}} = 4190$ K and $\log g = 4.31 \text{ cm s}^{-2}$ along with a veiling value at $1.6 \mu\text{m}$ of 0.11. From our Keck/HIRES spectra, we derive a spectral type of $K9.0 \pm 0.9$, which is between the M2 and the K6 that are implied by the two temperatures given above. We ultimately adopt the $M0.8 \pm 0.5$ found by Herczeg & Hillenbrand (2014) because, for M-type stars, spectral typing is considered more accurate at lower spectral resolution than higher. From adaptive-optics (AO)-resolved spectroscopy, V928 Tau A and B are found to have nearly identical near-infrared spectra (L. Prato 2020, private communication). Assuming the stars are in fact physically associated, the nearly identical spectra reinforce the notion that the two components have very similar bulk properties, such as mass and radius.

Radial and Rotational Velocity: Hartmann et al. (1986) first measured the radial velocity (18.3 km s^{-1}) and $v \sin i$ (24.9 km s^{-1}) for V928 Tau. Next, from four epochs of seeing-limited, high-resolution spectroscopy, Nguyen et al. (2012) measured the radial velocity to be $15.38 \pm 0.16 \text{ km s}^{-1}$ (with a weighted standard deviation of 1.67 km s^{-1} and systematic noise of 2.02 km s^{-1}). Those authors also measured $v \sin i$ to be $31.6 \pm 0.7 \text{ km s}^{-1}$.

Radial velocity data including the previous as well as our three new measurements are summarized in Table 3. Rotation data appear in Table 1. Other rotation measurements, in addition to those above, include Hartmann & Stauffer (1989) who reported $v \sin i = 18.8 \pm 3.3 \text{ km s}^{-1}$. From our Keck/HIRES data we determine a $v \sin i = 29 \pm 3 \text{ km s}^{-1}$ for the first, 2017 epoch; and $33.1 \pm 1.2 \text{ km s}^{-1}$ for the third, 2018 epoch. Kounkel et al. (2019) reported $v \sin i = 34.2 \pm 0.4 \text{ km s}^{-1}$ from APOGEE. We emphasize again that these measurements are for the combined (spatially unresolved) A and B stellar system. We also note that the various $v \sin i$ measurements were acquired with different spectral resolutions: $\sim 5 \text{ km s}^{-1}$ (Nguyen et al. 2012), $\sim 8 \text{ km s}^{-1}$ (this work), and $\sim 12\text{--}13 \text{ km s}^{-1}$ (Hartmann et al. 1986; Hartmann & Stauffer 1989; Kounkel et al. 2019). For comparison, the maximum velocity separation between the components for an assumed orbital period of 60 yr is 8 km s^{-1} .

2.2. Reddening

Herczeg & Hillenbrand (2014) measured the extinction toward V928 Tau from a flux-calibrated optical spectrum, finding $A_V = 1.95 \pm 0.2$ mag. This value is consistent with a local, high-resolution extinction map (Dobashi et al. 2005). Using the 2MASS extinction coefficients of Yuan et al. (2013) and assuming $R_V = 3.1$ (Cardelli et al. 1989), we calculated the extinction corrected near-infrared colors of the primary and secondary from the deblended photometry: $(J - K)_{0,\text{pri}} = 1.14 \pm 0.05$ mag and $(J - K)_{0,\text{sec}} = 1.21 \pm 0.05$ mag.

2.3. Stellar Parameters

From the veiling-corrected spectral type of Herczeg & Hillenbrand (2014) and its associated uncertainty, we determined T_{eff} via Monte Carlo error propagation and linear interpolation of Table 6 from Pecaut & Mamajek (2013),

Table 2
Astrometry for V928 Tau AB and Neighboring Tau IV Subgroup Members

ID	Catalog	ϖ (mas)	μ_α (mas yr ⁻¹)	μ_δ (mas yr ⁻¹)
V928 Tau	HSOY	...	5.816 ± 2.130	-29.200 ± 2.096
V928 Tau	GPS1	...	6.398 ± 1.823	-16.593 ± 1.532
V928 Tau	PPMXL	...	5.8 ± 4.5	-29.8 ± 4.5
2MASS J04321786+2422149	Gaia DR2	8.0534 ± 0.1915	6.255 ± 0.302	-22.196 ± 0.233
FY Tau	Gaia DR2	7.6798 ± 0.0710	6.651 ± 0.135	-21.855 ± 0.116
FZ Tau	Gaia DR2	7.6908 ± 0.0746	7.121 ± 0.143	-21.497 ± 0.106
Haro 6–13	Gaia DR2	7.6653 ± 0.1879	5.017 ± 0.317	-21.378 ± 0.243
HK Tau A	Gaia DR2	7.5005 ± 0.0924	4.464 ± 0.152	-22.961 ± 0.116
HK Tau B	Gaia DR2	5.1023 ± 1.5260	0.369 ± 2.520	-27.032 ± 2.032
2MASS J04325026+2422115	Gaia DR2	11.8560 ± 2.4075	7.042 ± 4.285	-25.073 ± 3.452
MHO 8	Gaia DR2	7.7979 ± 0.2219	6.369 ± 0.390	-20.474 ± 0.289
Tau IV	L09	7.14 ± 0.51	5.5 ± 1	-21.9 ± 1
median (Tau IV-V928)	this work	7.69 ± 0.06	6.13 ± 0.36	-22.03 ± 0.70
mean (Tau IV-V928)	this work	7.36 ± 0.36	6.31 ± 0.77	-22.20 ± 0.52

Note. The mean is the Chauvenet clipped mean. Uncertainties in the mean are the standard error. Uncertainties in the median are the uncertainty in the true median. References: Gaia DR2 = Gaia Collaboration et al. (2018). GPS1 = Tian et al. (2017). HSOY = Altmann et al. (2017). L09 = Luhman et al. (2009). PPMXL = Roeser et al. (2010).

Table 3
Radial Velocities of V928 Tau A+B

Date (JD)	Radial Velocity (km s ⁻¹)	References
...	18.3 ± 2.0^a	Hartmann et al. (1986)
...	15.38 ± 0.16	Nguyen et al. (2012)
...	7.71 ± 6.50	Gaia Collaboration et al. (2018)
...	16.1 ± 0.23	Kounkel et al. (2019)
...	18	Zhong et al. (2019)
2458032.11194	16.0 ± 1.8^b	this work
2458097.888854	14.4 ± 3.5^b	this work
2458425.83663	17.9 ± 2.8^b	this work

Notes.

^a The radial velocity uncertainty for the Hartmann et al. (1986) measurement has been estimated from Table 1 of that work.

^b Radial velocities derived from spatially unresolved spectroscopy of the blended binary.

appropriate for pre-main-sequence stars. Using the same table and methods, we determined the J -band bolometric correction, absolute J magnitude, bolometric magnitude, luminosity, and radius for each star (assuming the two stars have equivalent effective temperatures). We then performed a linear interpolation of the Dartmouth evolutionary models, both the standard Dotter et al. (2008) and magnetic Feiden (2016) versions, to determine masses and ages in the H-R diagram. Our derived stellar parameters are reported in Table 1.

2.4. Stellar Radii

While it is not clear which component of the binary is being transited or eclipsed, or whether the multiple dips observed by K2 and ground-based surveys may in fact be due to separate companions around both stars, our analysis is simplified somewhat by the fact that the two stars in the binary are nearly identical. From the two obvious rotation periods detected from K2 photometry and the $v \sin i$ value published in Nguyen et al. (2012), the minimum stellar radius can be

calculated as $R_* \sin i = 1.41 R_\odot$ or $1.56 R_\odot$, depending on which period is used (and ignoring differential rotation).

3. Observations

Here we summarize all the observations we collected on V928 Tau. Time-series photometry is from K2 and ground-based surveys, spectroscopy is from Keck I HIRES, and Gaia DR2 data and high-resolution imaging from Keck II NIRC2.

3.1. Time-series Photometry

3.1.1. K2

V928 Tau (EPIC 247795097) was observed by the Kepler space telescope between 2017 March 8 UT and 2017 May 27 UT during Campaign 13 of the K2 mission. The K2 light curve was extracted using the EVEREST 2.0 pipeline (Luger et al. 2016, 2018), which uses a variant of Pixel Level Decorrelation (PLD) to correct for the systematics in the Vanderburg & Johnson (2014) light curves. The light curve consists of 9344 observations, spanning ~ 80 days, with a Combined Differential Photometric Precision (CDPP) of ~ 113 ppm. This light curve is characterized by quasi-periodic brightness modulations, a beating pattern, and a deep asymmetric eclipse seen at BJD ~ 2457835 (see Figure 1). Using the `lightkurve` package (Lightkurve Collaboration et al. 2018), we extracted photometry from small apertures surrounding both V928 Tau and CFHT-BD-Tau 7, confirming that the dimming event in fact originates from V928 Tau. The asymmetric eclipse, after subtracting a stellar variability model and correcting for dilution due to the source binarity (as described in Section 4), is shown in Figure 2.

3.1.2. Photometry from Ground-based Surveys

To search for periodicity and long-term photometric variability of V928 Tau, we supplemented the K2 data with photometry from various ground-based surveys (see Figure 3). Information on each survey is listed in Table 4, and though Figure 3 shows several brightness minima for V928 Tau, not all are believed to be real. The most believable periods (visually

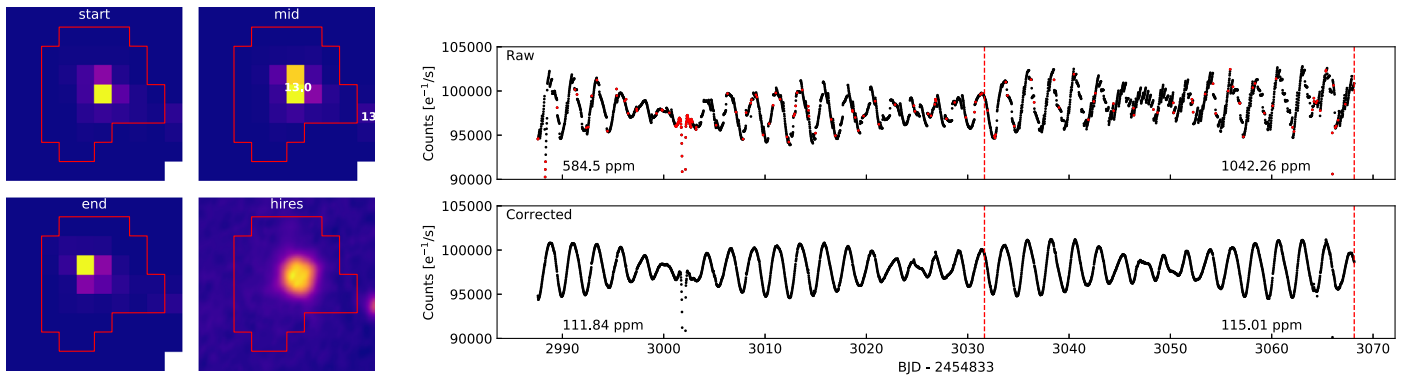


Figure 1. Left: the aperture used to compute the K2 light curve of V928 Tau with EVEREST 2.0. The high-resolution image in the lower-right panel is taken from the Palomar Observatory Sky Survey while the other images are from K2. Right: the raw (top) and corrected (bottom) K2 light curve of V928 Tau. Systematics were corrected using the Pixel Level Decorrelation (PLD) model of EVEREST 2.0. Red points were masked when computing the PLD model. Vertical red dashed lines indicate breakpoints. The Combined Differential Photometric Precision (CDPP) values on either side of the breakpoint are indicated in the lower portion of each panel. Note the eclipse occurring at BJD \sim 2457835 with a depth of \sim 30%.

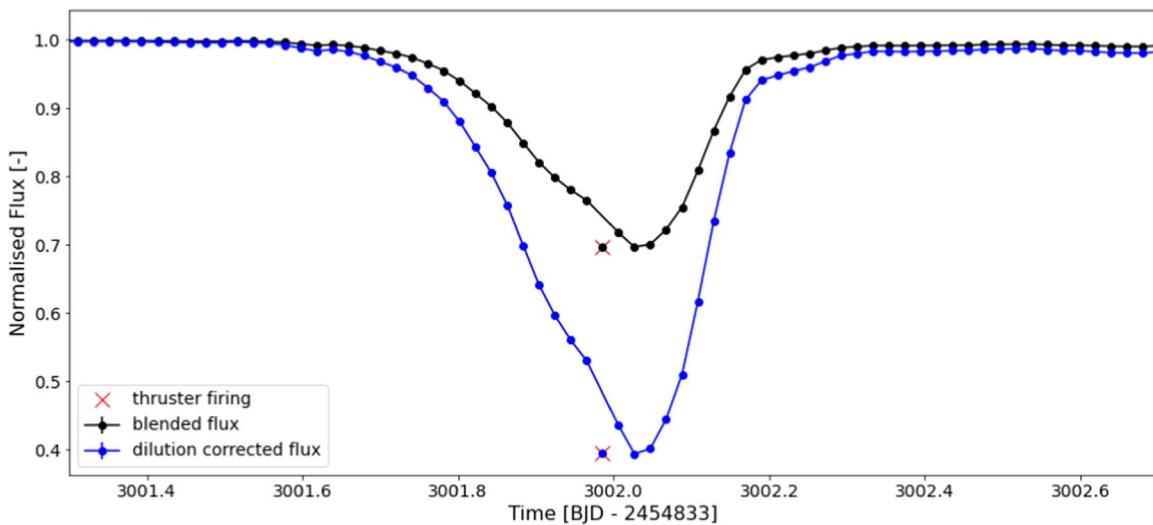


Figure 2. Light curve of V928 Tau after removing stellar variations centered on the eclipse. This figure shows the blended and dilution-corrected eclipse based on the assumption of two identical stars. A single observation during the eclipse was excluded due to a thrustor firing (marked with a red X).

determined), after applying period-folding and removing stellar variation, are depicted in Figure 4.

The photometry we gathered originates from the following time-domain surveys: the All Sky Automated Survey (ASAS; Pojmanski 1997), which consists of three separate telescopes at two locations, with a limiting magnitude of 13 mag and precision of 0.05 mag in the I band; the All Sky Automated Survey for Super-Novae (ASAS-SN; Shappee et al. 2014; Kochanek et al. 2017), which consists of five stations of four telescopes each, with a limiting magnitude of 17 mag; the Asteroid Terrestrial-impact Last Alert System (ATLAS; Heinze et al. 2018; Tonry et al. 2018), which consists of two telescopes with a limiting magnitude of about 19 mag; the Catalina Real-Time Transient Survey (CRTS, Drake et al. 2009), which consists of three telescopes with a limiting magnitude of 22 mag and take data without a filter; the Kilodegree Extremely Little Telescope (KELT; Pepper et al. 2007, 2012, 2018), which consists of two telescopes designed to observe V magnitudes between 7 and 11 mag with 1% precision, but capable of observing stars down to $V = 14$ mag; the Palomar Transient Factory (PTF; Law et al. 2009; Rau et al. 2009), which consists of one telescope for transient detection and one for photometric follow-up with a limiting magnitude of 20.6 mag in

the Mould- R band; the Super Wide-Angle Search for Planets (SWASP; Pollacco et al. 2006), which consists of 16 telescopes at two locations, designed to observe V magnitudes between 7.0 and 11.5 mag with 1% precision, but capable of observing stars down to $V = 15$ mag; and the Zwicky Transient Facility (ZTF; Bellm 2014), which expands on the PTF concept, consisting of a single telescope that has a limiting magnitude of 20.8 mag for the ZTF G band and 20.6 for the ZTF R band. Data were also collected from amateur astronomers Franz-Josef Hamsch (HMB), Sjoerd Dufoer (DFS), and Tonny Vanmunster (VMT), and the Astrolab Iris team (DUBF, Siegfried Vanaverbeke, Franky Dubois, Steve Rau, and Ludwig Logie).

Data from the amateur astronomers were obtained through the American Association for Variable Star Observers (AAVSO) website;²⁴ the ASAS-SN, ATLAS, CRTS, and ZTF surveys are publicly available from the project websites; the KELT light curve for V928 Tau was published in Rodriguez et al. (2017); and the data from SWASP and ASAS are made publicly available for the first time here.

²⁴ <https://www.aavso.org/main-data>

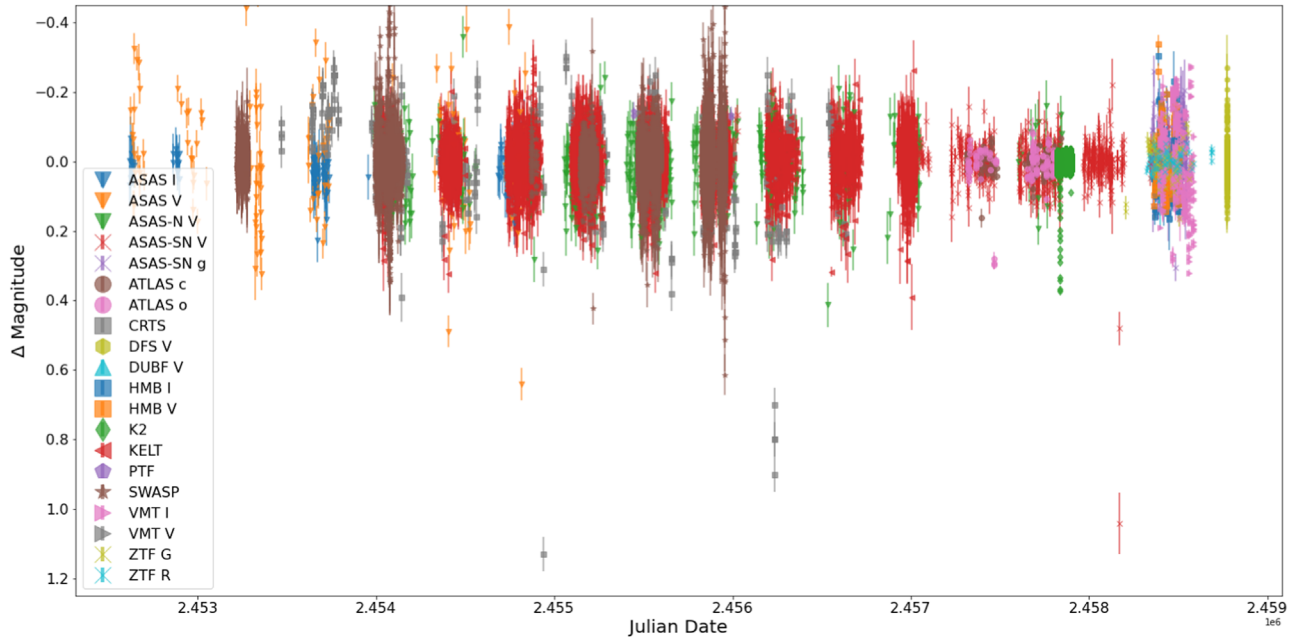


Figure 3. Time-series photometry of V928 Tau from several time-domain surveys. Note that data with magnitude errors exceeding 0.1 mag have been clipped for readability. Though there are several deep points, not all of these are believable dips. The most believable dips are shown in Figure 4 after period-folding the photometry.

Table 4
Ground Survey Information

Survey	Filter	n_{tel}	Baseline (days)	n_{phot}	Pixel Scale ($'' \text{ pix}^{-1}$)	Field of View ($\text{deg}^2 \text{ cam}^{-1}$)	Reduction (References)
ASAS ^a	<i>I</i>	1–3	2213	121	14.2	6.0, 77.4	Pojmanski (1997)
	<i>V</i>		2213	133			
	<i>V</i> ^b		3859	508			
ASAS-SN	<i>V</i>	8	2505	664	8.0	20.3	Kochanek et al. (2017)
	<i>g</i>	12	196	201			
ATLAS	<i>c</i>	8	527	132	1.9	28.9	Heinze et al. (2018)
	<i>o</i>		510	143			
CRTS	...	3	3168	412	2.5	8.0, 1.0, 4.2	Drake et al. (2009)
K2	K_p	1	81	3900	4.0	110	Luger et al. (2016, 2018)
KELT	R^c	2	2987	9888	23	676	Sivver et al. (2012)
PTF	<i>R</i>	1	547	4	1.0	8.1	Masci et al. (2016)
SWASP	<i>V</i>	16	2740	33704	13.7	64	Pollacco et al. (2006)
ZTF	<i>G</i>	1	370	63	1.0	47	Masci et al. (2018)
	<i>R</i>		363	67			
DFS	<i>V</i>	1	1	194	2.0	0.6	de Pontière (2010)
DUBF	<i>V</i>	1	46	63	1.9	0.1	Meng et al. (2017)
HMB	<i>I</i>	2	143	113	2.1, 2.2	0.6, 0.7	de Pontière (2010)
	<i>V</i>		143	118			
VMT	<i>I</i>	1	191	654	1.8	0.5	de Pontière (2010)
	<i>V</i>		2	7			

Notes.

^a Upgraded in 2002 from one to three telescopes in Chile.

^b Telescope in Hawaii.

^c Nonstandard; see Pepper et al. (2007).

We checked for additional photometric data from the DASCH digitized photographic plate archive (J. Grindlay 2020, private communication), the HATNet Exoplanet Survey (J. Hartman 2020, private communication), the Next Generation Transit Survey (E. Gillen 2020, private communication), and Evryscope (N. Law 2020, private communication). Unfortunately, data for

V928 Tau from these projects and surveys either do not presently exist or have not been processed.

A high-cadence light curve of <0.5 day duration from the Optical Monitor on board the XMM-Newton satellite was published in Audard et al. (2007). Not surprisingly, no eclipses were detected over that brief period.

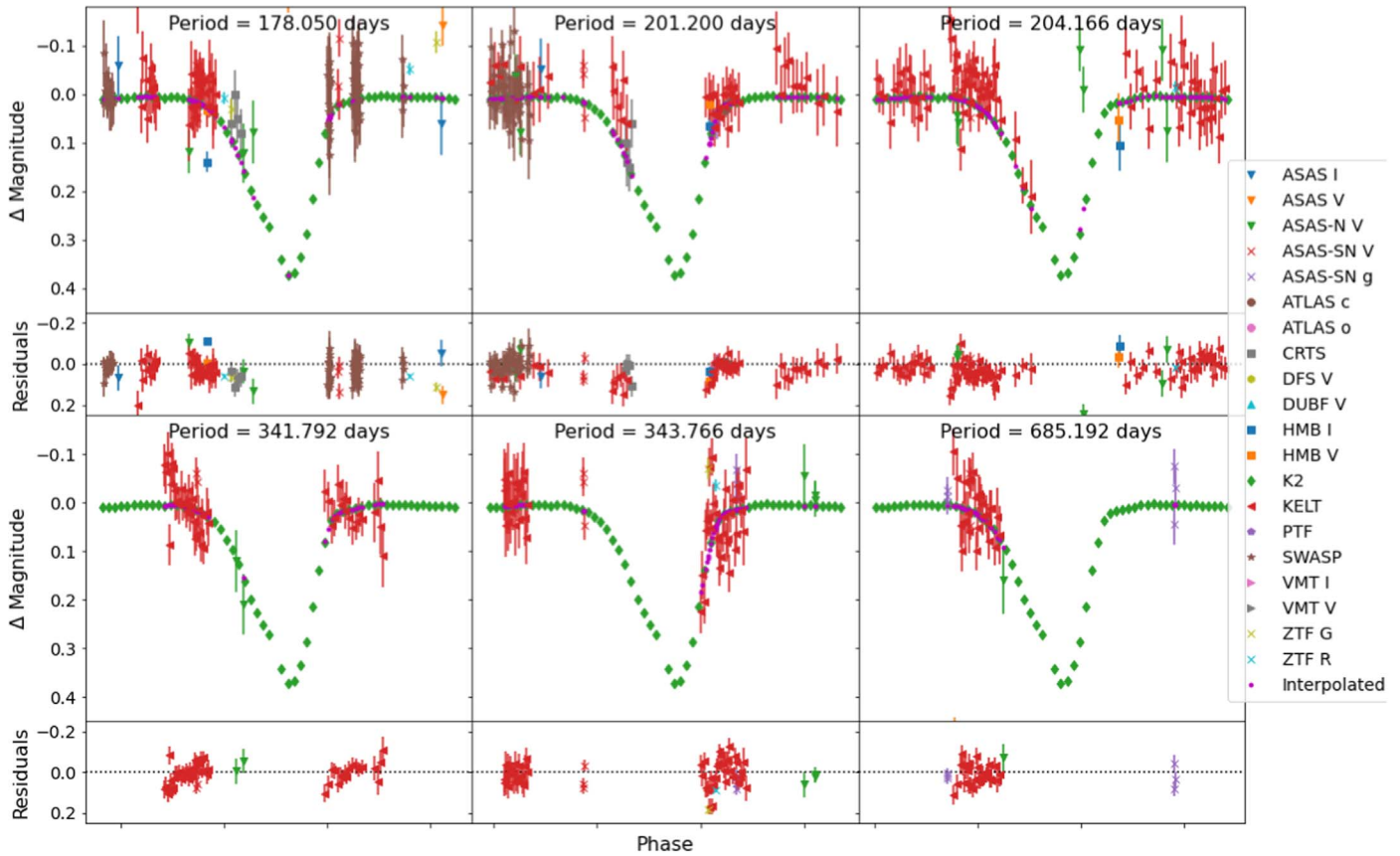


Figure 4. The photometry shown in Figure 3 is period-folded with a high-resolution period grid and then visually inspected near the eclipse to determine the most interesting periods. Most interesting means that there is a suggestion of another eclipse taking place with the given period. Note that the phase labels have been removed from the plot as they provide no interesting information.

3.2. Spectroscopy: Keck I/HIRES

We observed V928 Tau with the HIRES spectrograph (Vogt et al. 1994) at the Keck I telescope on 2017 October 5 UT, 2017 December 10 UT, and 2018 November 3 UT. For the first and third epochs, our HIRES reduction and analysis procedures are identical to those discussed in David et al. (2019). The radial velocity of the spatially and spectrally unresolved pair was determined from cross-correlation (Tonry & Davis 1979) of the spectrum with those of standard stars (Nidever et al. 2002) observed on the same night. The two measurements are formally consistent with one another. However, a better constraint on radial velocity variations comes from cross-correlating the observations with one another; this reveals an upper limit of $<1 \text{ km s}^{-1}$ on the difference in radial velocity at the two epochs. The cross-correlations are somewhat flat topped, but it was not possible to separate the signals from what is likely the two stellar components at approximately the same velocity. From the first-epoch spectrum, we also determined the sky-projected rotational velocity by artificially broadening a spectral standard using the Gray (2005) broadening profile, as well as the equivalent widths of the $H\alpha$, $H\beta$, and CaII H \& K lines, all of which are observed in emission. The third-epoch spectrum used a redder setting of HIRES and enabled us to measure Li I and also to note that the Ca II “infrared” triplet lines have subcontinuum core emission.

Our second epoch of HIRES observations were reduced and analyzed following the California Planet Search procedures outlined in Howard et al. (2010). The radial velocity at this epoch was determined using the telluric A and B absorption bands

as a wavelength reference (Chubak et al. 2012). While this method typically yields uncertainties of $0.1\text{--}0.3 \text{ km s}^{-1}$ for slowly rotating stars, we determined an uncertainty of 3.5 km s^{-1} from the rms of three-fourths of the spectral segments used to calculate the radial velocity.

3.3. Gaia DR2

Despite the brightness of V928 Tau, neither a parallax nor proper motions are available for the source from Gaia DR2 (ID 147799312239072000). This is likely a consequence of the source’s binarity, as indicated by the large values of the goodness-of-fit statistic of the astrometric model with respect to along-scan observations (137.8864) and the excess astrometric noise (4.218 mas , 3690σ). Gaia DR2 did, however, publish a radial velocity estimate with large relative uncertainty: $v_R = 7.71 \pm 6.50 \text{ km s}^{-1}$. V928 Tau’s low mass companion CFHT-Tau 7 ([MDM2001] CFHT-BD-Tau 7 = 2MASS J04321786 +2422149), associated as mentioned in Kraus & Hillenbrand (2009), at $18''$ separation is Gaia DR2 147799209159857280. Gaia DR2 reports a parallax $\varpi = 8.0534 \pm 0.1915 \text{ mas}$ and proper motion $\mu_\alpha, \mu_\delta = 6.255, -22.196 \pm (0.302, 0.233) \text{ mas yr}^{-1}$.

3.4. High-resolution Imaging: Keck II/NIRC2

We observed V928 Tau with infrared high-resolution AO imaging at Keck Observatory. The Keck Observatory observations were made with the NIRC2 instrument on Keck II behind the natural guide star AO system. The observations were made on

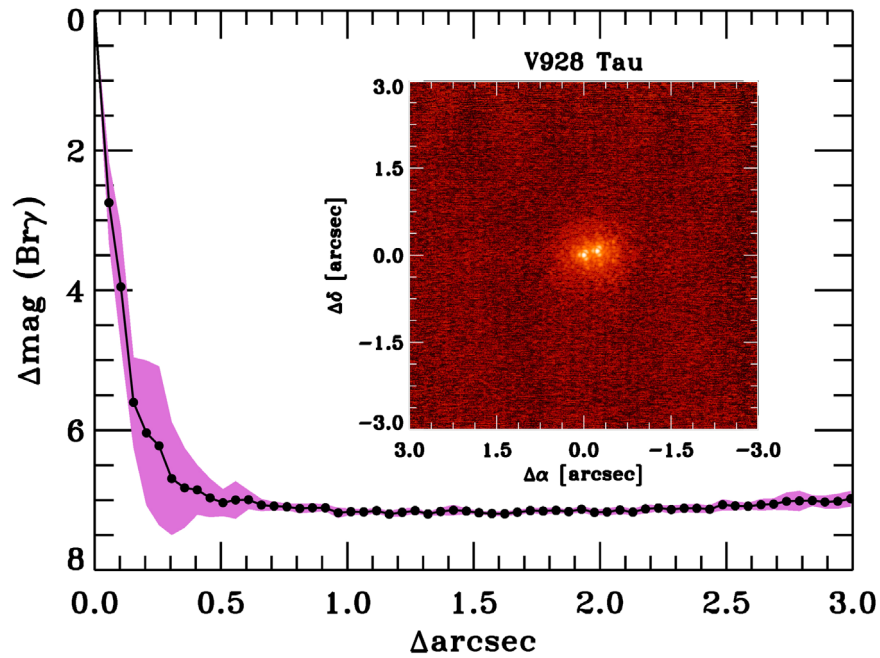


Figure 5. Companion sensitivity for the Keck adaptive-optics imaging in $\text{Br}\gamma$. The black points represent the 5σ limits and are separated in steps of 1 image FWHM ($\sim 0''.05$); the purple shading represents the azimuthal rms dispersion of the sensitivity. The wide dispersion in the $3\text{--}7 \lambda/D$ range is due to the directional dependence of the sensitivity due to the presence of the close secondary (V928 Tau B). The inset image is of the target clearly showing the resolved binary.

2017 September 11 UT in the standard three-point dither pattern that is used with NIRC2 to avoid the lower-left quadrant of the detector, which is typically noisier than the other three quadrants. The dither pattern step size was $3''$ and was repeated twice, with each dither offset from the previous dither by $0''.5$. The observations were made in the narrowband $\text{Br}\gamma$ filter ($\lambda_o = 2.1686 \mu\text{m}$; $\Delta\lambda = 0.0326 \mu\text{m}$) with an integration time of 2 s with one coadd per frame for a total of 18 s on target and in J_{cont} ($\lambda_o = 1.2132 \mu\text{m}$; $\Delta\lambda = 0.0198 \mu\text{m}$) with an integration time of 5 s with one coadd per frame for a total of 45 s on target. The camera was in the narrow-angle mode with a full field of view of $\sim 10''$ and a pixel scale of approximately $0''.0099442$ per pixel. The final combined dithers have a resolution of $0''.049$ in $\text{Br}\gamma$ and $0''.043$ in J_{cont} . The Keck AO observations clearly show the binary in both filters, with the stars having a difference in magnitude of $\Delta K = 0.069 \pm 0.006 \text{ mag}$ and $\Delta J = 0.122 \pm 0.014 \text{ mag}$. The observation also allows us to add another astrometric point to the emerging orbit for the stellar binary. There are no additional stellar companions brighter than about $\Delta K (\text{Br}\gamma) \approx 7 \text{ mag}$ (5σ) compared to the primary to within a resolution of $0''.1$ ($\sim 14 \text{ au}$; see Figure 5).

The sensitivities of the final combined AO image were determined by injecting simulated sources azimuthally around the primary target every 45° at separations of integer multiples of the central source’s FWHM (Furlan et al. 2017). The brightness of each injected source was scaled until standard aperture photometry detected it with 5σ significance. The resulting brightness of the injected sources relative to the target set the contrast limits at that injection location. The final 5σ limit at each separation was determined from the average of all of the determined limits at that separation. The uncertainty on the 5σ limit was set by the rms dispersion of the azimuthal slices at a given radial distance. The sensitivity curve is shown in Figure 5 along with an inset image zoomed to the primary target showing no other companion stars.

4. Light Curve Analysis

As observed by K2, V928 Tau is an unresolved, nearly equal-brightness binary. As such, the true eclipse depths are deeper by a factor dependent on the optical flux ratio and on which component is being eclipsed. Given the fact that the two stars are of similar spectral type, mass, and radius, we take the limiting case where both stars are identical.

4.1. Rotational Modulation

We interpret the brightness modulations as originating from starspots on the surfaces of the binary components, and the beating pattern as arising from the nearly equal rotation periods of the two stars (see Figure 6). Using a linear least-squares fit, we remove the linear trend ($m = 0.00001422$, $c = 0.99973174$). Using the Lomb–Scargle algorithm (Lomb 1976; Scargle 1982), we find four significant sinusoidal periods at 1.130, 1.245, 2.249, and 2.485 days. We note that if we accept a 1.0% discrepancy (i.e., the percentage offset between a perfect harmonic—in other words, an integer ratio): 2.249 and 2.485 days are the two independent fundamental periods, with 1.130 and 1.245 being the respective first harmonics. To determine the amplitudes and phases of these modulations, we use the Levenberg–Marquardt least-squares algorithm (Levenberg 1944; Marquardt 1963), removing elements one by one. We start with a linear trend with slope m and y intercept c , then two sinusoids, then again two sinusoids that have amplitudes a_x , periods P_x , and phases θ_x , where $x = 1, 2, 3, 4$. The least-squares fit provides an initial guess for the Markov Chain Monte Carlo (MCMC) simulation, and we run 250 chains with 10,000 links and a burn-in of 2000 steps. The results of the MCMC optimization are summarized in Table 5 and plotted in Figure 7. Note that there is no significant linear trend ($m = 0.00000224$, $c = 1.00022059$). P_1 (2.250 days) and P_2 (2.482 days) contain the largest power and are interpreted to be the probable rotation periods of the two stars, which are very similar to the rotation periods found by Rebull et al. (2020). P_3

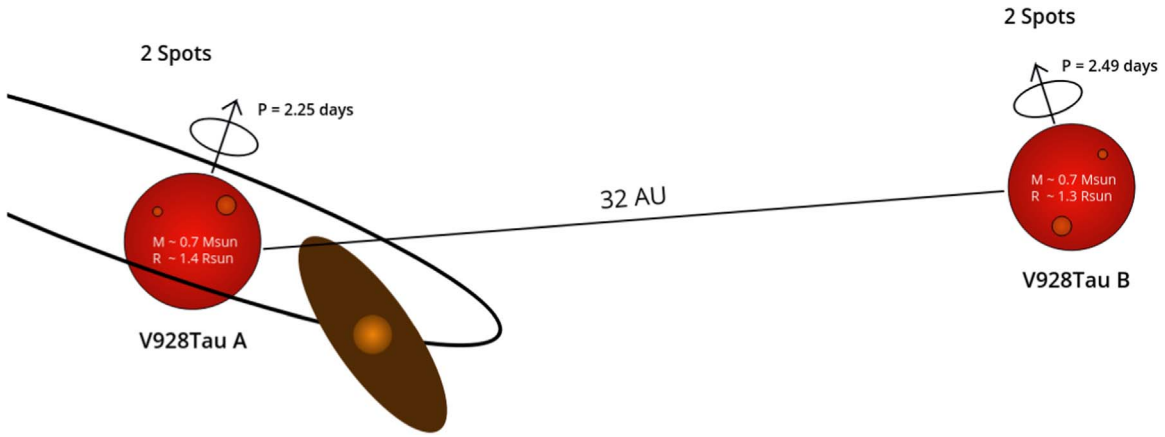


Figure 6. Interpretation of the K2 light curve of V928 Tau. The beating pattern arises from the rotational modulation of each star (due to starspots) with very similar periods. The deep, asymmetric eclipse is likely caused by a companion with a disk that is elliptical due to projection effects. Note: figure is not to scale or a sky projection (line of sight not necessarily into the page), rotational periods might correspond to opposite stars, and the proposed companion may orbit the other star.

Table 5
Sinusoidal Stellar Variations

Mode	Amplitude (%)	Period (days)	Phase (rad)	Harmonic Modes	Harmonic Discrepancy (%)
1	2.0	2.250	1.379
2	1.1	2.482	1.671
3	0.1	1.130	1.352	1	0.91
4	0.3	1.245	1.456	2	0.63

Note. Harmonic Modes indicate which modes are multiples of each other. Harmonic Discrepancy is the percentage off a perfect harmonic (e.g., with periods 1 and 2.1 days the harmonic discrepancy would be 10%).

and P_4 are the first harmonic of P_1 and P_2 , respectively (half periods), which are phase-shifted with respect to the fundamental periods producing the asymmetric features in the beating light curve. The exact physical reasons for this, whether it is a specific distribution of starspots, differential rotation or a combination of the two, is not relevant to this study as it is focused on characterizing the eclipse, and the stellar variation model residuals are small ($<0.5\%$). Examining the ground-based data does not convincingly confirm or reject the stellar variation model determined by the K2 data. This is likely due to the low amplitude of the modulation, the relatively high uncertainties on ground measurements, and the likelihood that the stellar activity (spots and phases) evolves with time on the surface of the star.

4.2. Eclipse Fitting

We note that the eclipse observed in the K2 photometry is most likely the result of the occulter eclipsing a single component of V928 Tau. Usually, one would have to make separate models for the transit along either star, but given the fact that the two stars are of similar spectral type, mass, and radius, we take the limiting case where both stars are identical. In this case, we simply double the fluctuations about the median (of one) and obtain the deblended light curve of V928 Tau A/B (see Figure 2). After correction for the true eclipse depth, we find that the eclipse depth exceeds 50%.

Other systems that show similar lopsided eclipses include EE Cephei, the similar ϵ Aurigae, and TYC 2505-672-1. These are the only known long-period eclipsing binary star systems with

obscurations caused by a large dust disk surrounding one of the components. EE Cephei has not been observed directly, but extensive modeling was done by Gařan et al. (2012) and later tested with an international observing campaign by Pieńkowski et al. (2020). ϵ Aurigae on the other hand was observed directly using Georgia State University’s Center for High Angular Resolution Astronomy Interferometer (CHARA; ten Brummelaar et al. 2005) using the Mid Infra-Red Combiner (MIRC; Monnier et al. 2010) and modeled extensively (Kloppenborg et al. 2010, 2015). Rodriguez et al. (2016) found TYC 2505-672-1, an M-type red giant that undergoes a ~ 3.45 yr long, near-total eclipse every 69.1 yr due to a moderately hot (~ 8000 K) object with a large circumstellar disk, by sifting through 120 yr worth of light curves. Other interesting systems are OGLE LMC-ECL-11893 (Scott et al. 2014) and OGLE-BLG182.1.162852 (Rattenbury et al. 2014), which are modeled as circumstellar disks of an unseen companion transiting the primary.

The depth and asymmetry of the deblended V928 Tau eclipse make it very unlikely that the eclipse is caused by another star, in an equatorial orbit. Instead, this gives rise to the theory that the eclipse is caused by an inclined and tilted disk around an unseen object, which, due to projection, produces an elliptical occulter.

This disk is modeled as an azimuthally symmetric dust disk with radius R_d , disk inclination i , tilt (angle with respect to the orbital path) ϕ , impact parameter (with respect to the orbital path) b , and an opacity, τ . For matters of simplicity, we assume the projection of the occulter can be modeled as a disk (no gap between body and disk, or companion bulge). To model the eclipse, the linear limb-darkening parameter u , of the star and the transverse velocity of the disk v_t , are required (R_* is needed to convert v_t from $R_* \text{ day}^{-1}$ to km s^{-1}). The models for u are dependent on the effective temperature T_{eff} , metallicity $[\text{Fe}/\text{H}]$, surface gravity $\log g$, and microturbulence velocity v_{turb} . Tottle & Mohanty (2015) find that $T_{\text{eff}} = 3525$ K. Padgett (1996) and D’Orazi et al. (2011) find that the $[\text{Fe}/\text{H}]$ of stars in the Taurus-Aurigae association are near solar (<0.1), so we assume $[\text{Fe}/\text{H}] = 0.0$. In the models of limb darkening, v_{turb} is restricted to 2 km s^{-1} , leaving $\log g$ to be inferred. We can estimate $\log g$ using Equation (1), where M_* and R_* are the mass and radius of the star, respectively, and $\log g_{\odot} \sim 4.44 \text{ cm s}^{-2}$ (using IAU nominal values), based on the radii and masses given

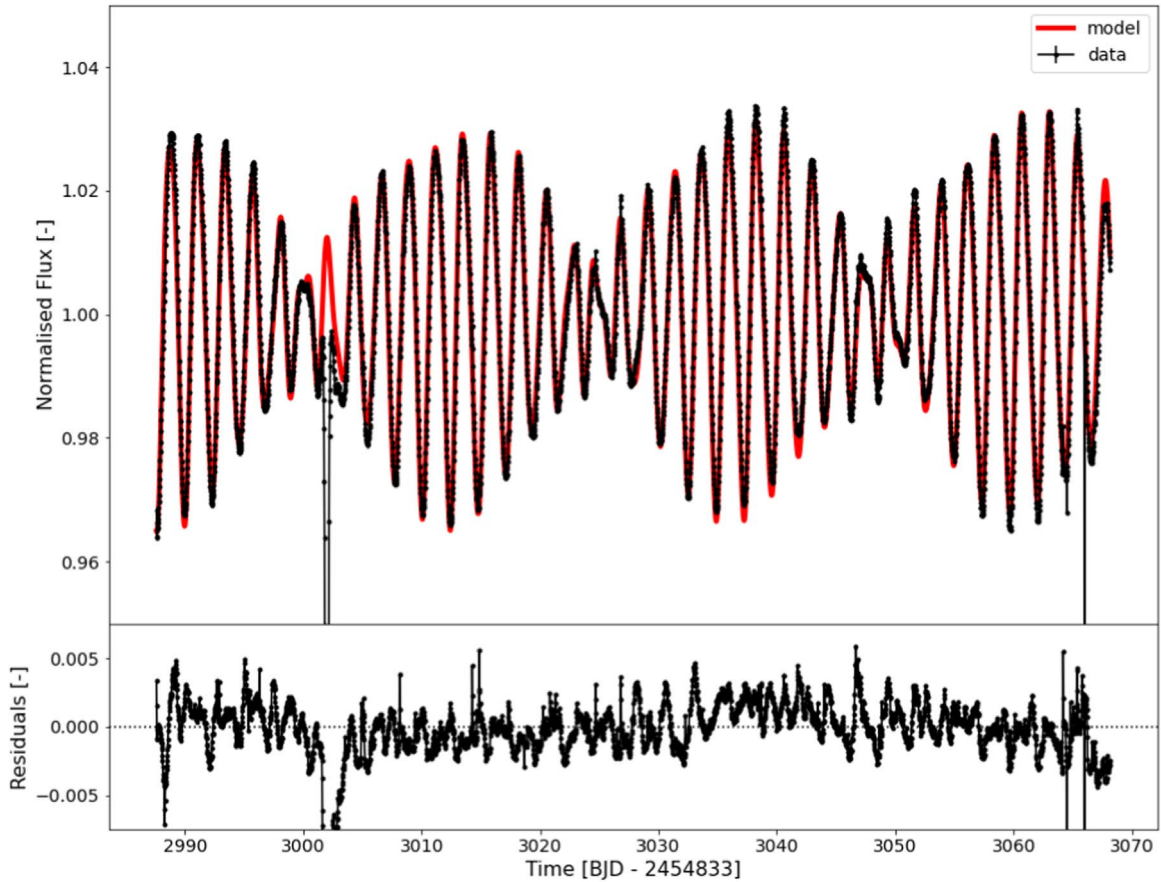


Figure 7. Top: light curve for V928 Tau obtained from the `everest 2.0` pipeline with the best-fit MCMC model for the stellar modulations superimposed. Bottom: residuals of the fit.

in Table 1,

$$\log g = \log g_{\odot} + \log \frac{M_{*}}{M_{\odot}} - 2 \log \frac{R_{*}}{R_{\odot}}. \quad (1)$$

Corrections due to rotational velocity of the stars are negligible as they are a small fraction of the breakup velocity ($\sim 13\%$). We use the `jktd` Fortran code developed by Southworth (2015) to linearly interpolate (T_{eff} and $\log g$) the tables from Sing (2010) for values of u for the Kepler bandpass in each of the four cases (V928 Tau A and B, with Dartmouth standard and magnetic models). We take u to be the average of these four cases, giving $u = 0.7220$. Given u , we can ensure the v_t predicted by the MCMC sampling algorithm is physical by following the method of van Werkhoven et al. (2014) to derive a lower limit for the speed of the occulting object by measuring the steepest time derivative of the light curve \dot{L} , (the egress) and assuming the radius R , for each star with u ,

$$v_t = \dot{L} R \pi \left(\frac{2u - 6}{12 - 12u + 3\pi u} \right). \quad (2)$$

Using these values of u , the sizes of each star and the luminosity slope of the egress, $\dot{L} = 4.19 L_{*} \text{ day}^{-1}$, we obtain a lower limit of $v_{t,A} = 65.5 \text{ km s}^{-1}$, $v_{t,B} = 61.7 \text{ km s}^{-1}$, which is consistent with the best-fit v_t . This corresponds to $\sim 5.91 R_{*}$.

As there are likely many acceptable configurations, we try to find the smallest disk that could cause the eclipse, the reason

being that this can provide lower-mass limits on the companion, and can constrain the disk size, in the most intuitive way. We do this in two ways: modeling a partially transmitting disk, which is preferentially opaque (τ from 0.5 to 1.0) and a fully opaque disk ($\tau = 1$).

To perform the modeling of the elliptical occulter, we use a modified version of the `pyPplusS` code developed by Rein & Ofir (2019). This code produces light curves in physical space, i.e., it determines the eclipse depth based on the physical area that has been blocked by the occulter (which can be a planet, disk, or planet disk/ring system combination of which we use the disk model). This produces photometric points based on the geometry and location of the occulter with respect to the host star as well as the limb-darkening model of the star, which in this case we simplify to the linear model with parameter u . Note further that this code works in units of stellar radii, which permits us to ignore the choice of star and the uncertainties on the radii. However, to produce a light curve, it is necessary to convert the spatial domain to the temporal domain by introducing v_t and fitting for the time of maximum occultation δt , with respect to $\text{BJD} = 2457835$.

We start off by initializing a set of 1000 chains for 3500 links with the initial bounds as described in Table 6 and bind the probability by the parameter bounds. We further check to make sure that all the initial chains produce a transit (otherwise it might be too far removed to converge to a given solution), and as a final check, we determine whether the system is physical. The math and limits to determine whether or not a set

Table 6
MCMC Boundaries

Parameter	Parameter Bounds	Initial Walker Bounds	Units
R_d	0–10	0–5	R_*
b	–10–10	–5–5	R_*
i	0–90	45–90	deg
ϕ	0–90	0–90	deg
v_t	5.9–20	5.9–10	$R_* \text{ day}^{-1}$
δt	–10–10	–0.5–0.5	day
τ	0–1	0.5–1	

Note. Notes on the parameter bounds. (1) The upper bound for R_d has been deemed large enough. (2) The bounds for b are such that the disk must transit the star. (3) Due to reflection symmetries caused by the combination of b and ϕ , ϕ is limited from 0° to 90° instead of -180° to 180° . (4) The lower bound for v_t corresponds to the method discussed in van Werkhoven et al. (2014), with an upper bound deemed large enough.

of model parameters produces a physical disk is described in detail in Section 4.4, but the basic concept is as follows. A disk is considered physical if $R_d < 0.3 r_H$, where r_H is the Hill radius of the companion. We can determine the physical upper limit of R_d by maximizing r_H through the selection of the smallest possible host mass M_* , and the largest possible companion mass M_p and periastron passage r_{peri} . M_* is the same for the magnetic models of V928 Tau A and B; for M_p we use $80 M_{\text{Jup}}$, which is an upper limit for the deuterium-burning limit; and the largest stable r_{peri} depends on the largest stable apastron passage r_{ap} , for which we use an upper limit of 3.2 au (this is 10% of the binary separation, which fulfills an orbital stability criterion). With these criteria and by selecting V928 Tau B (this maximizes r_{peri}) because of its smaller radius R_* , the physicality of the disk is solely determined by v_t of the disk model.

Performing the MCMC optimization reveals several local minima for the eclipse solutions, namely a high-velocity set ($v_t > 8 R_* \text{ day}^{-1}$, 381 chains, burn-in 500 links) and a low-velocity set with small disk radii ($v_t < 8 R_* \text{ day}^{-1}$ and $R_d < 1.5 R_*$, 472 chains, burn-in 1000 links). We also find that in both cases the opaque disk produces a better fit than the translucent disk, so we scrap the translucent solutions. The results of the MCMC optimization are summarized in Table 7 (Opaque Fast and Opaque Slow columns) and visualized in Figure 8 (orange and green lines respectively). Note that the errors displayed in the table are on the MCMC distribution itself, whereas the systematic errors are much larger. Examples of these errors include uncertainties in u , R_* , the assumption that the two stars are identical so the deblended light curve is as depicted in Figure 2. Also consider the fact that this model does not include the scattering of light and other such processes that would influence the shape of the light curve.

4.3. Two-component Disk Model

We also attempt a two-component fuzzy disk model where we add two parameters to the model, namely the thickness of the second (edge) component t_e and its opacity τ_e . Note that the total radius of the fuzzy disk is the sum of R_d and t_e . We run the same procedure described in Section 4.2 with these two additional parameters with the additional constraint that $\tau_e < \tau$. Performing the MCMC optimization reveals two local minima

for the eclipse solutions, namely a high-velocity set ($v_t > 8.5 R_* \text{ day}^{-1}$, 446 chains, burn-in 2500 links) and a low-velocity set ($v_t < 8.5 R_* \text{ day}^{-1}$, 554 chains, burn-in 1000 links). The results of the MCMC sampling are summarized in Table 7 (Fuzzy Fast and Fuzzy Slow columns) and visualized in Figure 8 (red and purple lines respectively). Due to the significantly higher v_t , we adopt the single, low-velocity, small-radius opaque disk model (opaque slow).

4.4. Periodicity

The eclipse observed by K2 does not repeat over the baseline of those observations. Because the eclipse occurs during the first half of the K2 campaign, a lower limit on a potential period is obtained from $P_{\text{orb}} > t_{\text{K2,end}} - t_{\text{ecl}} - t_{\text{dur}}$, where P_{orb} is the orbital period, $t_{\text{K2,end}}$ is the final time stamp from K2, t_{ecl} is the eclipse midpoint, and t_{dur} is the eclipse duration. In this case, the period of the candidate eclipsing companion must be $P_{\text{orb}} > 66$ days.

We construct models on the orbit and periodicity of the proposed companion. We initially assume that v_t corresponds to a circular orbit, leading to a semimajor axis $a \sim 0.1$ au and $P_{\text{orb}} < 66$ days—given that no other eclipse is seen, this rules out circular orbits for the occulter. The orbit must therefore be eccentric, and to investigate possible orbits, we assume that $v_t = v_{\text{peri}}$, where v_{peri} is the periastron velocity, and explore a grid containing M_p and P_{orb} .

We determine an upper bound for M_p given that the spectra of the both components of the binary are nearly identical and that there is no obvious tertiary companion in the high-spatial-resolution images (see Figure 5). To do this, we take the upper-mass limit of substellar objects, i.e., the deuterium-burning limit. Despite the fact that more recent studies by Baraffe et al. (2015) and Forbes & Loeb (2019) show that the deuterium-burning limit is 73–74 M_{Jup} , we take the older upper limit of 80 M_{Jup} determined by Saumon & Marley (2008) to be inclusive of higher masses. Quarles et al. (2020) find that for a companion to remain bound to its host in a binary star system with a_{bin} , the orbit of the companion must have $a/a_{\text{bin}} < 0.08$ for a prograde orbit. For a retrograde orbit, this fraction increases to 0.10. By taking the upper limit of 10%, which results in $a = 3.2$ au, we find that $P_{\text{orb}} = 2.8$ yr for a circular orbit. Thus, P_{orb} is run from 66 days to 2.8 yr.

With a fixed mass of the host M_* , $v_t = v_{\text{peri}}$, and a grid of M_p and P_{orb} , we can determine the eccentricity e , and r_{peri} , which we require to determine r_H and r_{ap} . We do this as follows. We use Kepler’s third law to determine, a . Using a we can determine e by isolating it from the equation for v_{peri} (Equation (3), where $\mu = G(M_* + M_p)$):

$$v_{\text{peri}} = \sqrt{\frac{(1-e)\mu}{(1+e)a}}. \quad (3)$$

Using e and a , we can determine r_{peri} and r_{ap} , and finally, we use r_{peri} to estimate r_H as shown in Equation (4):

$$r_H = r_{\text{peri}} \sqrt{\frac{M_p}{3(M_* + M_p)}}. \quad (4)$$

For a disk to be stable over extended periods of time $r_d < 0.3 r_H$. Given that the companion will spend a significant fraction of its orbital period at r_{ap} , we constrain the system by requiring that $r_{\text{ap}} < 3.2$ au as the orbit must remain stable. This

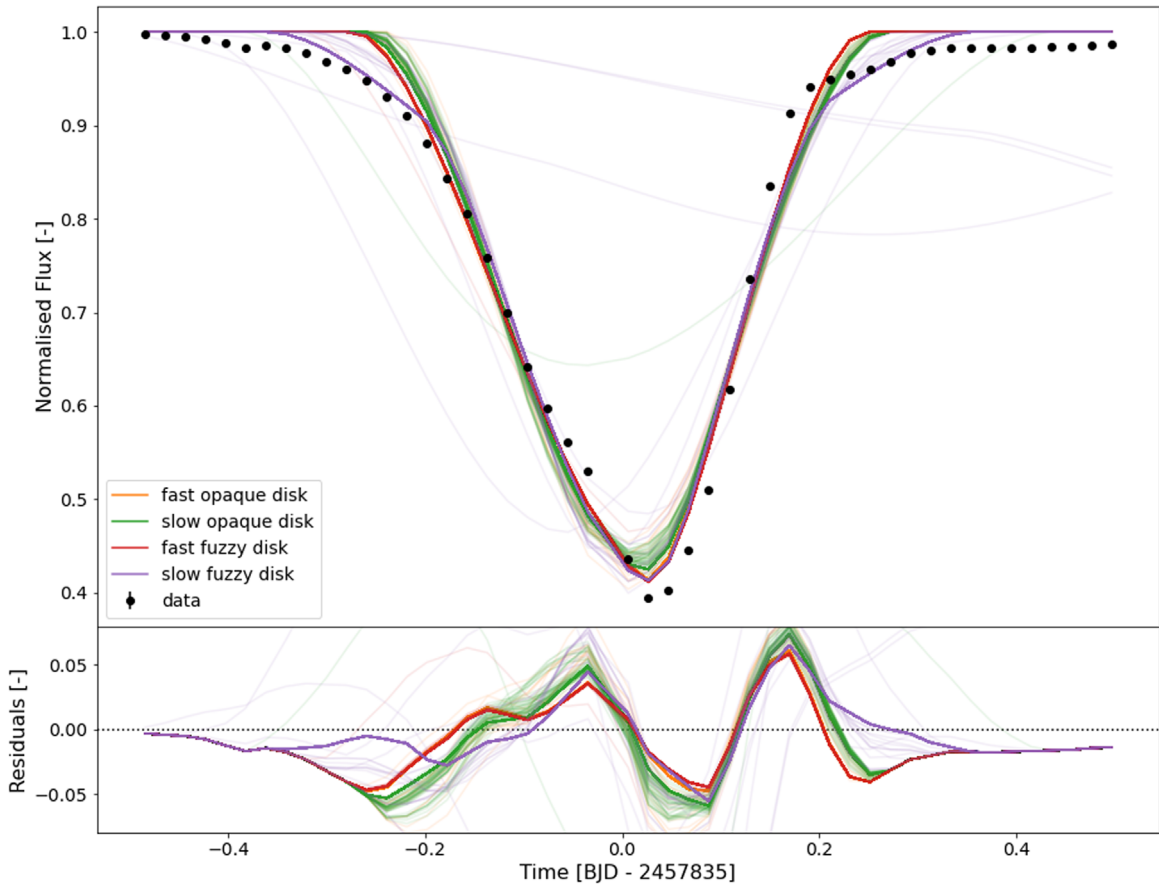


Figure 8. Top: results of the MCMC sampling algorithm for the different local minima for the single-component opaque disk model in orange ($v_t > 8 R_* \text{ day}^{-1}$) and green ($v_t < 8 R_* \text{ day}^{-1}$ and $R_d < 1.5 R_*$) and the two-component fuzzy disk model in red ($v_t > 8.5 R_* \text{ day}^{-1}$) and purple ($v_t < 8.5 R_* \text{ day}^{-1}$) for the eclipse of V928 Tau with the best-fit parameters summarized in Table 7. Bottom: residuals of the MCMC samples. Note that the “fast opaque disk” and the “fast fuzzy disk” practically overlap.

Table 7
Eclipse Model Parameters

Parameter	Opaque Fast	Opaque Slow	Fuzzy Fast	Fuzzy Slow
$R_d (R_*)$	1.9392 ± 0.0005	0.9923 ± 0.0005	2.2265 ± 0.0485	0.9900 ± 0.0004
$t_e (R_*)$	0.0515 ± 0.0515	1.7440 ± 0.0018
$b (R_*)$	0.8519 ± 0.0007	-0.2506 ± 0.0002	0.8285 ± 0.0022	-0.3130 ± 0.0003
$i (^\circ)$	67.1137 ± 0.0141	56.7817 ± 0.0262	64.6010 ± 0.0319	59.9468 ± 0.0167
$\varphi (^\circ)$	24.8334 ± 0.0195	41.2197 ± 0.0496	41.1384 ± 0.0830	38.8399 ± 0.0511
v_t	$(R_* \text{ day}^{-1})$	9.1354 ± 0.0013	6.6367 ± 0.0018	9.2005 ± 0.0066
	8.3637 ± 0.0030	$v_{t,A} (\text{kms}^{-1})$	101.22 ± 0.02	73.53 ± 0.02
	101.94 ± 0.08	92.67 ± 0.04		
$v_{t,B} (\text{kms}^{-1})$	95.33 ± 0.02	69.26 ± 0.02	96.01 ± 0.07	87.28 ± 0.04
δt (day)	-0.0586 ± 0.0001	0.0099 ± 0.0000	-0.0589 ± 0.0002	0.0164 ± 0.0000
τ (-)	1.0	1.0	0.646 ± 0.001	1.000 ± 0.000
τ_e (-)	0.646 ± 0.127	0.154 ± 0.001

Note. The total size of the disk is the sum of R_d and t_e . For the conversion of v_t to km s^{-1} we use $R_* = 1.376 R_\odot$ for $v_{t,A}$ and $R_* = 1.296 R_\odot$ for $v_{t,B}$ corresponding to the radii of V928 Tau A and B.

method, with the given constraints, reveals that the opaque fast model requires $M_p > 50 M_{\text{jup}}$; the fuzzy fast and fuzzy slow models require $M_p > 78 M_{\text{jup}}$. We thus adopt the opaque slow model for which the parameter maps are shown in Figure 9 for the magnetic models of V928 Tau.

This figure shows that the r_{ap} constraint limits P_{orb} to ~ 1000 days for the magnetic models. The r_{H} constraint carves out the region at the bottom of the maps so the minimum M_p increases as P_{orb} decreases.

5. Astrometric Analysis

We used astrometry compiled from the literature and our newly acquired data point from NIRC2 to fit plausible Keplerian orbits to the data. The relative astrometry between V928 Tau A and B are found in Table 8.

Our analysis closely follows the exoplanet (Foreman-Mackey et al. 2020) tutorial available online.²⁵ After an initial

²⁵ <https://docs.exoplanet.codes/en/stable/tutorials/astrometric/>

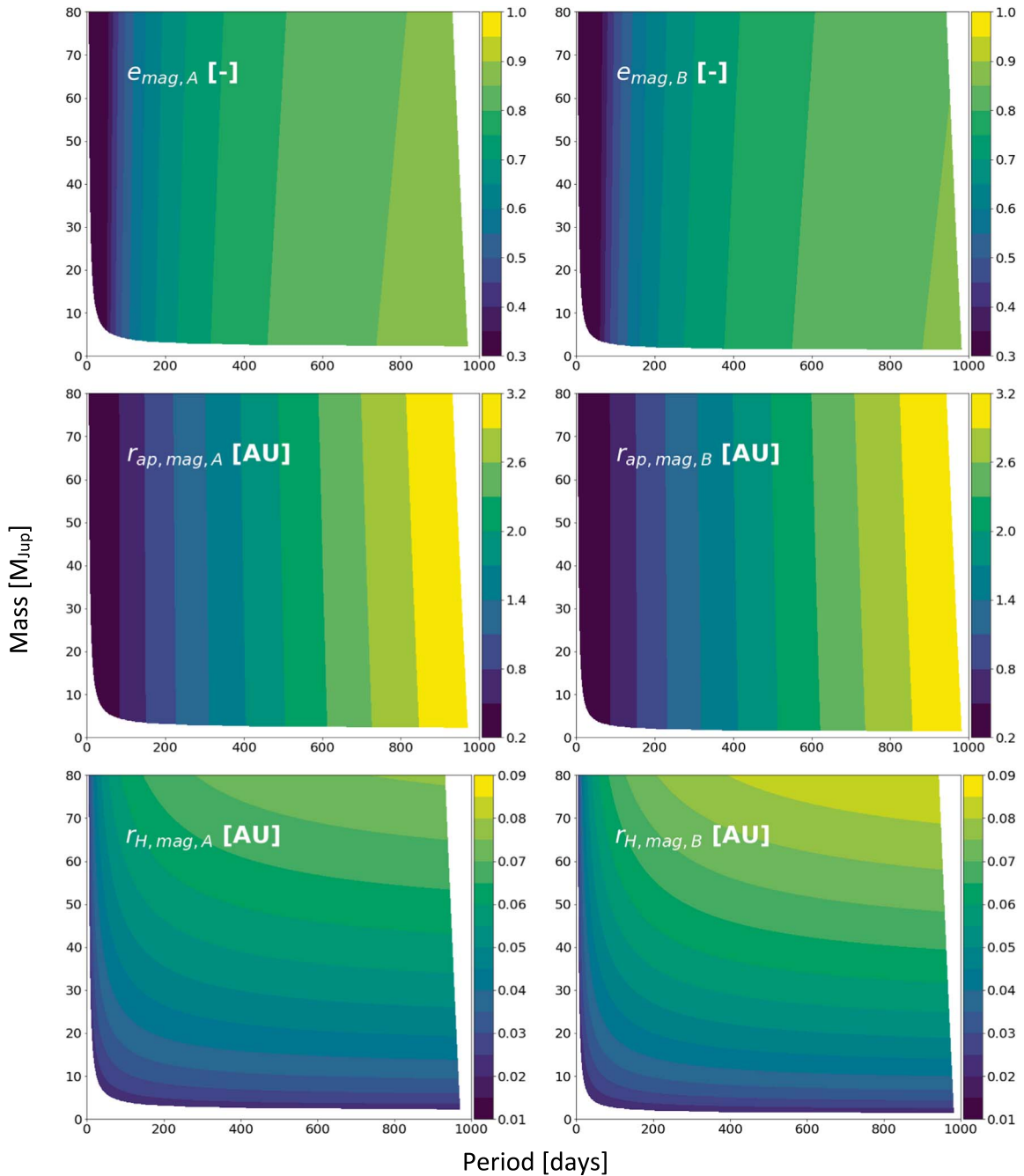


Figure 9. Parameter spaces mapped out for the opaque slow disk model with a companion mass M_p , and orbital period P_{orb} grid for the magnetic models of V928 Tau A and B (see Table 1). Left and right panels show the properties if the companion orbits either V928 Tau A or B, respectively. From top to bottom, the properties mapped are eccentricity e (-), apastron distance r_{ap} (au), and the Hill radius r_{H} (au). The bottom of each parameter map is masked out due to the r_{H} constraint ($r_{\text{disk}} < 0.3 r_{\text{H}}$). The right side of each parameter map is masked out due to the r_{ap} constraint ($r_{\text{ap}} < 0.10 a_{\text{bin}}$).

optimization with `scipy.optimize.minimize` using the Broyden–Fletcher–Goldfarb–Shanno (BFGS) method to find the maximum a posteriori solution we sampled from the posterior distribution using `exoplanet` and `PyMC3` (Salvati et al. 2016). The free parameters of the model were the log of the orbital period ($\log P$), $p = (\Omega + \omega)/2$, $m = (\Omega - \omega)/2$, eccentricity (e), cosine of the inclination ($\cos i$), a phase angle, the projected semimajor axis in arcseconds (a), the parallax (ϖ), and jitter terms for the angular separation and position angle ($\log s_p$ and $\log s_\theta$). We assumed Gaussian priors on the total system mass ($\mu = 1.4 M_\odot$, $\sigma = 0.1 M_\odot$) and the parallax ($\mu = 8.0534$ mas, $\sigma = 0.1915$ mas). Because the data only

cover a small fraction of the orbit, we sampled only to get a coarse understanding of the posterior distribution and did not sample until convergence (for example, the Gelman–Rubin statistic for the orbital period was 1.02). We used four chains with 10,000 links and a burn-in of 5000 steps, for a final chain length of 20,000. Nevertheless, from this preliminary sampling, we determined that the 68% (99.7%) highest posterior density interval for the orbital period is 73–171 (67–597) yr. Our lower bound on the orbital period of the binary (>67 yr at 99.7% confidence) is somewhat larger than the minimum period of 58 yr found by Schaefer et al. (2014) using the same data without our most recent measurement. The time-series astrometry and

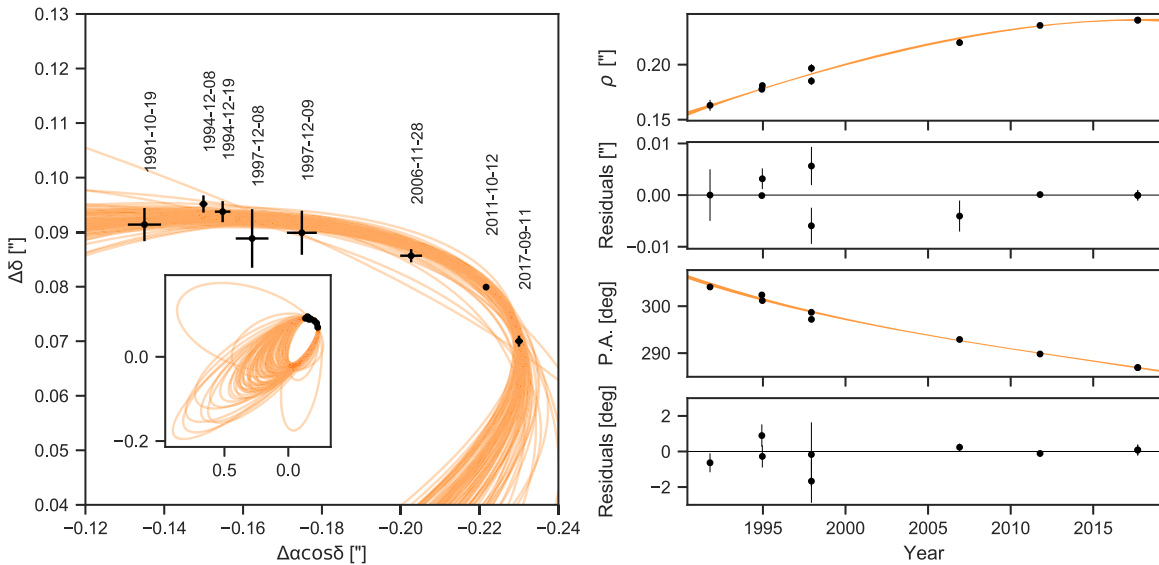


Figure 10. Relative astrometry of V928 Tau A and B. Left: the orbit of V928 Tau B as it appears on the sky, with V928 Tau A at the origin (outside the plot range). Random draws from the posterior are shown by the orange curves. The inset panel shows the full orbit. Upper right: time series of angular separation measurements (above) and residuals (below). Lower right: time series of position angle measurements (above) and residuals (below).

Table 8
Relative Astrometry of V928 Tau A and B

Date (UT)	ρ (")	P.A. (deg.)	Flux Ratio	Band	References
...	0.18 ± 0.01	300 ± 4	0.88 ± 0.03	<i>K</i>	Leinert et al. (1993)
1991-10-19	0.163 ± 0.005	304.1 ± 0.5	...	<i>K</i>	Ghez et al. (1995)
1994-12-8	0.1776 ± 0.0002	302.4 ± 0.6	1.0 ± 0.1	<i>V</i>	Simon et al. (1996)
1994-12-19	0.181 ± 0.002	301.2 ± 0.6	...	<i>K</i>	Ghez et al. (1995)
1997-12-8	0.1851 ± 0.0035	298.7 ± 1.8	1.009 ± 0.002	<i>L</i>	White & Ghez (2001)
1997-12-9	0.1967 ± 0.0037	297.2 ± 1.2	1.055 ± 0.037	<i>K</i>	White & Ghez (2001)
2006-11-28	0.220 ± 0.003	292.92 ± 0.09	0.9728 ± 0.0089	<i>K'</i>	Kraus & Hillenbrand (2012)
2011-10-12	0.23562 ± 0.00012	289.827 ± 0.031	0.9751 ± 0.0058	<i>K</i> _{cont}	Schaefer et al. (2014)
2017-09-11	0.24042 ± 0.00099	286.93 ± 0.24	0.938 ± 0.026	<i>K</i> _s	this work
			0.893 ± 0.025	<i>J</i>	this work

Note. We have added 180° to the position angles reported by Ghez et al. (1995), Simon et al. (1996), and White & Ghez (2001) for consistency with the other surveys. A precise date was not given for the Leinert et al. (1993) measurement so we did not include it in our astrometric analysis.

model fits drawn from the posterior are shown in Figure 10. The inferred parameters of the astrometric fit are summarized in Table 9. Future modeling with longer astrometric and radial velocity time series should better constrain the binary’s orbit.

6. Discussion

We find a model (opaque slow) for a companion orbiting either V928 Tau A or B with a surrounding dust disk with size $\sim 0.99 R_*$, which is $\sim 1.36 R_\odot$ for V928 Tau A and $\sim 1.28 R_\odot$ for V928 Tau B, which is significantly smaller than the proposed dust disk for J1407 (Kenworthy & Mamajek 2015) and EPIC 204376071 (Rappaport et al. 2019), nevertheless significantly larger than the expected radius for Roche rings (e.g., Saturn’s rings). This is the case for both absolute size and relative size (compared to R_*). We kept the model as simple as possible, but a larger number of degrees of freedom (i.e., a ring system, with varying opacities, or an attenuating disk) can always result in a better fit. Another feature to note in the model is the difficulty in modeling the “wings” of the eclipse. These can be partially justified with a transition from transparent to opaque along the disk

edge, but this results in an unphysically large edge. One could imagine that an attenuating disk model could solve this with a size between the single-component hard disk model and the two-component fuzzy disk model and could thus be a physical disk.

We argue that the companion should be on a highly eccentric orbit and relatively high mass, up to a brown dwarf ($80 M_{\text{Jup}}$). The implied nonzero eccentricity seems to support a trend as we find that J1407 ($e > 0.7$) and EPIC 204376071 ($e > 0.33$) both require eccentric orbits to explain the lack of other eclipses in their light curves, implying that the companion disk plays an important role in planetary dynamics and could play a major role in the dynamical evolution of planet formation. If this trend is discovered in other systems, it implies that the circumplanetary disk may play a role in the migration of the companion. Bowler et al. (2020) show that directly imaged brown dwarfs have a preference for higher eccentricities (in line with J1407) and gas giants have a strong preference for small eccentricities (EPIC 204376071 is in conflict with this result). Winn & Fabrycky (2015) show that the distribution of e tends to focus on small values for short periods, broadening at longer periods.

Table 9
Results of Astrometric Fit

Variable	Mean	Std. dev.	Highest Posterior Density 3%	Highest Posterior Density 97%
<i>Sampled</i>				
$\log P$	10.897	0.510	10.175	11.823
$\log s_p$	-9.563	3.206	-15.652	-5.122
$\log s_\theta$	-5.952	1.329	-7.450	-4.175
a (")	0.266	0.103	0.149	0.465
p (rad)	1.668	0.305	1.185	2.048
m (rad)	-0.006	0.357	-0.514	0.635
phase (rad)	0.171	2.085	-2.899	3.126
$\cos i$	-0.267	0.116	-0.511	-0.148
e	0.554	0.169	0.336	0.928
ϖ (mas)	8.028	0.192	7.672	8.391
<i>Derived</i>				
P (yr)	171.090	107.930	70.860	370.898
a (au)	33.119	12.904	18.773	57.695
t_{peri}	2454177.322	16129.837	2428221.544	2471110.331
Ω (deg)	95.913	33.232	36.497	139.630
ω (deg)	95.283	18.507	76.146	105.711
i (deg)	105.711	7.334	98.549	120.722












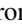





Further discoveries of other disk and ring systems, and confirmation of the orbital periods of these known systems will resolve this observation. We selected a disk with the highest opacity for the occulter, but of course, there is a family of companion disks, which have the same eclipse profile but are larger in diameter. These run into the issue of stability within the Hill sphere, as explored by Rieder & Kenworthy (2016) for J1407. Follow-up observations of this particular system would allow us to further characterize it and determine its composition through multifilter observations (and thus the grain-size distribution), along with high-resolution spectra to determine the chemical composition of the surrounding disk and companion. V928 Tau is a particularly hard system to detect as the eclipse length is approximately half a day, allowing the eclipse to be hidden by the diurnal cycle. Further modeling of the stellar variation spanning the whole baseline of observations (including the full activity cycle of the star) could reveal hints of another eclipse, providing potential periods for predictions of the next transit event. Follow-up observations that either confirm the existence of the occulters or that detect other eclipses in these systems will help us understand the nature of these intriguing systems.

We thank Dan Foreman-Mackey, Ian Czekala, and Sarah Blunt for helpful discussions on the astrometric modeling. This paper includes data collected by the Kepler mission and obtained from the MAST data archive at the Space Telescope Science Institute (STScI). Funding for the Kepler mission is provided by the NASA Science Mission Directorate. STScI is operated by the Association of Universities for Research in Astronomy, Inc., under NASA contract NAS 526555. Part of this research was carried out at the Jet Propulsion Laboratory, California Institute of Technology, under a contract with the National Aeronautics and Space Administration (80NM0018D0004). T.J.D. and E.E.M. gratefully acknowledge support from the Jet Propulsion Laboratory Exoplanetary Science Initiative and NASA award 17-K2G06-0030. Some of the data presented herein were obtained

at the W. M. Keck Observatory from telescope time allocated to the National Aeronautics and Space Administration through the agency's scientific partnership with the California Institute of Technology and the University of California. The Observatory was made possible by the generous financial support of the W. M. Keck Foundation. The authors wish to recognize and acknowledge the very significant cultural role and reverence that the summit of Maunakea has always had within the indigenous Hawaiian community. We are most fortunate to have the opportunity to conduct observations from this mountain. This work has made use of data from the Asteroid Terrestrial-impact Last Alert System (ATLAS) project. ATLAS is primarily funded to search for near-Earth asteroids through NASA grants NN12AR55G, 80NSSC18K0284, and 80NSSC18K1575; by-products of the NEO search include images and catalogs from the survey area. The ATLAS science products have been made possible through the contributions of the University of Hawaii Institute for Astronomy, the Queen's University Belfast, the Space Telescope Science Institute, and the South African Astronomical Observatory.

Software: EVEREST (v2.0; Luger et al. 2016, 2018), lightcurve (v1.9.0; Lightkurve Collaboration et al. 2018), exoplanet (Foreman-Mackey et al. 2020), PyMC3 (v3.8; Salvatier et al. 2016), Scipy (v1.4.1; Virtanen et al. 2020), Matplotlib (v3.2.2; Hunter 2007), Astropy (v4.0; Astropy Collaboration et al. 2013; Price-Whelan et al. 2018), Numpy (v1.18.1; Harris et al. 2020), jktld (v3.0; Southworth 2015).

ORCID iDs

Dirk M. van Dam  <https://orcid.org/0000-0002-1033-3461>
 Matthew A. Kenworthy  <https://orcid.org/0000-0002-7064-8270>
 Trevor J. David  <https://orcid.org/0000-0001-6534-6246>
 Eric E. Mamajek  <https://orcid.org/0000-0003-2008-1488>
 Ann Marie Cody  <https://orcid.org/0000-0002-3656-6706>
 Andrew W. Howard  <https://orcid.org/0000-0001-8638-0320>
 Howard Isaacson  <https://orcid.org/0000-0002-0531-1073>
 David R. Ciardi  <https://orcid.org/0000-0002-5741-3047>
 Luisa M. Rebull  <https://orcid.org/0000-0001-6381-515X>
 John R. Stauffer  <https://orcid.org/0000-0003-3595-7382>
 Rahul Patel  <https://orcid.org/0000-0002-5025-6827>
 Andrew Collier Cameron + WASP Collaborators  <https://orcid.org/0000-0002-8863-7828>
 Joseph E. Rodriguez  <https://orcid.org/0000-0001-8812-0565>
 Grzegorz Pojmański  <https://orcid.org/0000-0002-6495-0676>
 Erica J. Gonzales  <https://orcid.org/0000-0002-9329-2190>
 Joshua E. Schlieder  <https://orcid.org/0000-0001-5347-7062>
 Siegfried Vanaverbeke  <https://orcid.org/0000-0003-0231-2676>

References

- Alam, S., Albareti, F. D., Prieto, C. A., et al. 2015, *ApJS*, **219**, 12
 Alencar, S. H. P., Teixeira, P. S., Guimarães, M. M., et al. 2010, *A&A*, **519**, A88
 Altmann, M., Roeser, S., Demleitner, M., Bastian, U., & Schilbach, E. 2017, *A&A*, **600**, L4
 Ansdell, M., Gaidos, E., Hedges, C., et al. 2019a, *MNRAS*, **492**, 572
 Ansdell, M., Gaidos, E., Jacobs, T. L., et al. 2019b, *MNRAS*, **483**, 3579
 Armitage, P. J. 2011, *ARA&A*, **49**, 195
 Astropy Collaboration, Robitaille, T. P., Tollerud, E. J., et al. 2013, *A&A*, **558**, A33
 Audard, M., Briggs, K. R., Grosso, N., et al. 2007, *A&A*, **468**, 379
 Baraffe, I., Homeier, D., Allard, F., & Chabrier, G. 2015, *A&A*, **577**, A42
 Bellm, E. 2014, in The Third Hot-wiring the Transient Universe Workshop, ed. P. R. Wozniak et al. (Washington, DC: Los Alamos National Laboratory), 27

- Borucki, W. J., Koch, D., Basri, G., et al. 2010, *Sci*, **327**, 977
- Bowler, B. P., Blunt, S. C., & Nielsen, E. L. 2020, *AJ*, **159**, 63
- Cardelli, J. A., Clayton, G. C., & Mathis, J. S. 1989, *ApJ*, **345**, 245
- Chubak, C., Marcy, G., Fischer, D. A., et al. 2012, arXiv:1207.6212
- Cody, A. M., & Hillenbrand, L. A. 2018, *AJ*, **156**, 71
- Cody, A. M., Stauffer, J., Baglin, A., et al. 2014, *AJ*, **147**, 82
- Cohen, M., & Kuhl, L. V. 1979, *ApJS*, **41**, 743
- D'Orazi, V., Biazzo, K., & Randich, S. 2011, *A&A*, **526**, A103
- David, T. J., Hillenbrand, L. A., Gillen, E., et al. 2019, *ApJ*, **872**, 161
- de Pontière, P. 2010, LESVEPHOTOMETRY, Automatic Photometry Software, <http://www.dppobservatory.net>
- Dent, W. R. F., Thi, W. F., Kamp, I., et al. 2013, *PASP*, **125**, 477
- Dobashi, K., Uehara, H., Kandori, R., et al. 2005, *PASJ*, **57**, S1
- Dotter, A., Chaboyer, B., Jevremović, D., et al. 2008, *ApJS*, **178**, 89
- Drake, A. J., Djorgovski, S. G., Mahabal, A., et al. 2009, *ApJ*, **696**, 870
- Feiden, G. A. 2016, *A&A*, **593**, A99
- Feigelson, E. D., & Kriss, G. A. 1983, *AJ*, **88**, 431
- Forbes, J. C., & Loeb, A. 2019, *ApJ*, **871**, 227
- Foreman-Mackey, D., Luger, R., Czekala, I., et al. 2020, exoplanet-dev/exoplanet, v0.3.2, Zenodo, doi:10.5281/zenodo.1998447
- Furlan, E., Ciardi, D. R., Everett, M. E., et al. 2017, *AJ*, **153**, 71
- Gaia Collaboration, Brown, A. G. A., Vallenari, A., et al. 2018, *A&A*, **616**, A1
- Gaġan, C., Mikolajewski, M., Tomov, T., et al. 2012, *A&A*, **544**, A53
- Ghez, A. M., Neugebauer, G., & Matthews, K. 1993, *AJ*, **106**, 2005
- Ghez, A. M., Weinberger, A. J., Neugebauer, G., Matthews, K., & McCarthy, D. W., Jr. 1995, *AJ*, **110**, 753
- Gomez, M., Hartmann, L., Kenyon, S. J., & Hewett, R. 1993, *AJ*, **105**, 1927
- Gray, D. F. 2005, *The Observation and Analysis of Stellar Photospheres* (3rd ed.; Cambridge: Cambridge Univ. Press)
- Guieu, S., Dougados, C., Monin, J.-L., Magnier, E., & Martín, E. L. 2006, *A&A*, **446**, 485
- Handler, G. 2013, in *Planets, Stars and Stellar Systems*, ed. T. D. Oswalt & M. A. Barstow (Dordrecht: Springer), 207
- Harris, C. R., Jarrod Millman, K., & van der Walt, S. J. 2020, arXiv:2006.10256
- Hartmann, L., Hewett, R., Stahler, S., & Mathieu, R. D. 1986, *ApJ*, **309**, 275
- Hartmann, L., & Stauffer, J. R. 1989, *AJ*, **97**, 873
- Heinze, A. N., Tonry, J. L., Denneau, L., et al. 2018, *AJ*, **156**, 241
- Herczeg, G. J., & Hillenbrand, L. A. 2014, *ApJ*, **786**, 97
- Howard, A. W., Johnson, J. A., Marcy, G. W., et al. 2010, *ApJ*, **721**, 1467
- Howell, S. B., Sobeck, C., Haas, M., et al. 2014, *PASP*, **126**, 398
- Hunter, J. D. 2007, *CSE*, **9**, 90
- Joncour, I., Duchêne, G., & Moraux, E. 2017, *A&A*, **599**, A14
- Joncour, I., Duchêne, G., Moraux, E., & Motte, F. 2018, *A&A*, **620**, A27
- Jones, B. F., & Herbig, G. H. 1979, *AJ*, **84**, 1872
- Joy, A. H. 1945, *ApJ*, **102**, 168
- Kennedy, G. M., Kenworthy, M. A., Pepper, J., et al. 2017, *RSOS*, **4**, 160652
- Kenworthy, M. A., & Mamajek, E. E. 2015, *ApJ*, **800**, 126
- Kenyon, S. J., Brown, D. I., Tout, C. A., & Berlind, P. 1998, *AJ*, **115**, 2491
- Kley, W., & Nelson, R. P. 2012, *ARA&A*, **50**, 211
- Kloppenborg, B., Stencel, R., Monnier, J. D., et al. 2010, *Natur*, **464**, 870
- Kloppenborg, B. K., Stencel, R. E., Monnier, J. D., et al. 2015, *ApJS*, **220**, 14
- Kochanek, C. S., Shappee, B. J., Stanek, K. Z., et al. 2017, *PASP*, **129**, 104502
- Kounkel, M., Covey, K., Moe, M., et al. 2019, *AJ*, **157**, 196
- Kraus, A. L., & Hillenbrand, L. A. 2009, *ApJ*, **703**, 1511
- Kraus, A. L., & Hillenbrand, L. A. 2012, *ApJ*, **757**, 141
- LaCourse, D. M., & Jacobs, T. L. 2018, *RNAAS*, **2**, 28
- Law, N. M., Kulkarni, S. R., Dekany, R. G., et al. 2009, *PASP*, **121**, 1395
- Leinert, C., Zinnecker, H., Weitzel, N., et al. 1993, *A&A*, **278**, 129
- Levenberg, K. 1944, *QApMa*, **2**, 164
- Lightkurve Collaboration, Cardoso, J. V. d. M., Hedges, C., et al. 2018, Lightkurve: Kepler and TESS time series analysis in Python, Astrophysics Source Code Library, ascl:1812.013
- Lomb, N. R. 1976, *Ap&SS*, **39**, 447
- Luger, R., Agol, E., Kruse, E., et al. 2016, *AJ*, **152**, 100
- Luger, R., Kruse, E., Foreman-Mackey, D., Agol, E., & Saunders, N. 2018, *AJ*, **156**, 99
- Luhman, K. L., Mamajek, E. E., Allen, P. R., & Cruz, K. L. 2009, *ApJ*, **703**, 399
- Marquardt, D. W. 1963, *J. Soc. Ind. Appl.*, **11**, 431
- Martin, E. L., Rebolo, R., Magazzu, A., & Pavlenko, Y. V. 1994, *A&A*, **282**, 503
- Masci, F. J., Laher, R. R., Rebbapragada, U. D., et al. 2016, *PASP*, **129**, 014002
- Masci, F. J., Laher, R. R., Rusholme, B., et al. 2018, *PASP*, **131**, 018003
- Meng, H. Y. A., Rieke, G., Dubois, F., et al. 2017, *ApJ*, **847**, 131
- Monnier, J. D., Anderson, M., Baron, F., et al. 2010, *Proc. SPIE*, **7734**, 77340G
- Nguyen, D. C., Brandeker, A., van Kerkwijk, M. H., & Jayawardhana, R. 2012, *ApJ*, **745**, 119
- Nidever, D. L., Marcy, G. W., Butler, R. P., Fischer, D. A., & Vogt, S. S. 2002, *ApJS*, **141**, 503
- Olah, K., Kővári, Z., Bartus, J., et al. 1997, *A&A*, **321**, 811
- Osborn, H. P., Kenworthy, M., Rodriguez, J. E., et al. 2019, *MNRAS*, **485**, 1614
- Osborn, H. P., Rodriguez, J. E., Kenworthy, M. A., et al. 2017, *MNRAS*, **471**, 740
- Padgett, D. L. 1996, *ApJ*, **471**, 847
- Pecaut, M. J., & Mamajek, E. E. 2013, *ApJS*, **208**, 9
- Pepper, J., Kuhn, R. B., Siverd, R., James, D., & Stassun, K. 2012, *PASP*, **124**, 230
- Pepper, J., Pogge, R. W., DePoy, D. L., et al. 2007, *PASP*, **119**, 923
- Pepper, J., Stassun, K. G., & Gaudi, B. S. 2018, in *Handbook of Exoplanet*, ed. H. Deeg & J. Belmonte (Cham: Springer), 128
- Pierikowski, D., Gaġan, C., Tomov, T., et al. 2020, *A&A*, **639**, A23
- Pojmanski, G. 1997, *AcA*, **47**, 467
- Pollacco, D. L., Skillen, I., Collier Cameron, A., et al. 2006, *PASP*, **118**, 1407
- Price-Whelan, A. M., Sipőcz, B. M., Günther, H. M., et al. 2018, *AJ*, **156**, 123
- Quarles, B., Li, G., Kostov, V., & Haghighipour, N. 2020, *AJ*, **159**, 80
- Rappaport, S. 2012, Possible Disintegrating Short-Period Super-Mercury Orbiting KIC 12557548, HST Proposal, 12987
- Rappaport, S., Zhou, G., Vanderburg, A., et al. 2019, *MNRAS*, **485**, 2681
- Rattenbury, N. J., Wyrzykowski, Ł., Kostrzewa-Rutkowska, Z., et al. 2014, *MNRAS*, **447**, L31
- Rau, A., Kulkarni, S. R., Law, N. M., et al. 2009, *PASP*, **121**, 1334
- Rebull, L. M., Stauffer, J. R., Cody, A. M., et al. 2020, *AJ*, **159**, 273
- Rein, E., & Ofir, A. 2019, *MNRAS*, **490**, 1111
- Ridden-Harper, A. R., Keller, C. U., Min, M., van Lieshout, R., & Snellen, I. A. G. 2018, *A&A*, **618**, A97
- Rieder, S., & Kenworthy, M. A. 2016, *A&A*, **596**, A9
- Rodono, M., Cutispoto, G., Pazzani, V., et al. 1986, *A&A*, **165**, 135
- Rodriguez, J. E., Ansdell, M., Oelkers, R. J., et al. 2017, *ApJ*, **848**, 97
- Rodriguez, J. E., Stassun, K. G., Lund, M. B., et al. 2016, *AJ*, **151**, 123
- Roeser, S., Demleitner, M., & Schilbach, E. 2010, *AJ*, **139**, 2440
- Salvatier, J., Wiecki, T. V., & Fonnesbeck, C. 2016, PyMC3: Python Probabilistic Programming Framework, v3.8, Astrophysics Source Code Library, ascl:1610.016
- Saumon, D., & Marley, M. S. 2008, *ApJ*, **689**, 1327
- Scargle, J. D. 1982, *ApJ*, **263**, 835
- Schaefer, G. H., Prato, L., Simon, M., & Patience, J. 2014, *AJ*, **147**, 157
- Scott, E. L., Mamajek, E. E., Pecaut, M. J., et al. 2014, *ApJ*, **797**, 6
- Shappee, B. J., Prieto, J. L., Grupe, D., et al. 2014, *ApJ*, **788**, 48
- Simon, M., Holfeltz, S. T., & Taff, L. G. 1996, *ApJ*, **469**, 890
- Sing, D. K. 2010, *A&A*, **510**, A21
- Siverd, R. J., Beatty, T. G., Pepper, J., et al. 2012, *ApJ*, **761**, 123
- Skrutskie, M. F., Cutri, R. M., Stiening, R., et al. 2006, *AJ*, **131**, 1163
- Southworth, J. 2015, JKTL: Limb Darkening Coefficients, v3.0, Astrophysics Source Code Library, ascl:1511.016
- Strom, K. M., Strom, S. E., Edwards, S., Cabrit, S., & Skrutskie, M. F. 1989, *AJ*, **97**, 1451
- Teachey, A., Kipping, D. M., & Schmitt, A. R. 2018, *AJ*, **155**, 36
- ten Brummelaar, T. A., McAlister, H. A., Ridgway, S. T., et al. 2005, *ApJ*, **628**, 453
- Tian, H.-J., Gupta, P., Sesar, B., et al. 2017, *ApJS*, **232**, 4
- Tognelli, E., Prada Moroni, P. G., & Degl'Innocenti, S. 2011, *A&A*, **533**, A109
- Tonry, J., & Davis, M. 1979, *AJ*, **84**, 1511
- Tonry, J. L., Denneau, L., Heinze, A. N., et al. 2018, *PASP*, **130**, 064505
- Tottle, J., & Mohanty, S. 2015, *ApJ*, **805**, 57
- van Dam, D., Kenworthy, M., David, T., et al. 2019, AAS/ESS Abstracts, **51**, 322.10
- van Lieshout, R., & Rappaport, S. A. 2018, in *Handbook of Exoplanets*, ed. H. Deeg & J. Belmonte (Cham: Springer), 1527
- van Werkhoven, T. I. M., Kenworthy, M. A., & Mamajek, E. E. 2014, *MNRAS*, **441**, 2845
- Vanderburg, A., & Johnson, J. A. 2014, *PASP*, **126**, 948
- Virtanen, P., Gommers, R., Oliphant, T. E., et al. 2020, *NatMe*, **17**, 261
- Vogt, S. S., Allen, S. L., Bigelow, B. C., et al. 1994, *Proc. SPIE*, **2198**, 362
- White, R. J., & Ghez, A. M. 2001, *ApJ*, **556**, 265
- Winn, J. N., & Fabrycky, D. C. 2015, *ARA&A*, **53**, 409
- Wright, E. L., Eisenhardt, P. R. M., Mainzer, A. K., et al. 2010, *AJ*, **140**, 1868
- Yuan, H. B., Liu, X. W., & Xiang, M. S. 2013, *MNRAS*, **430**, 2188
- Zacharias, N., Finch, C., Subasavage, J., et al. 2015, *AJ*, **150**, 101
- Zhong, J., Li, J., Carlin, J. L., et al. 2019, *ApJS*, **244**, 8